Photonic Events with Missing Energy in e^+e^- Collisions at $\sqrt{s} = 189$ GeV

The OPAL Collaboration

Abstract

Photonic events with large missing energy have been observed in e^+e^- collisions at a centre-of-mass energy of 189 GeV using the OPAL detector at LEP. Results are presented for event topologies consistent with a single photon or with an acoplanar photon pair. Cross-section measurements are performed within the kinematic acceptance of each selection, and the number of light neutrino species is measured. Cross-section results are compared with the expectations from the Standard Model process $e^+e^- \to \nu\bar{\nu}$ + photon(s). No evidence is observed for new physics contributions to these final states. Upper limits on $\sigma(e^+e^- \to XY) \cdot BR(X \to Y\gamma)$ and $\sigma(e^+e^- \to XX) \cdot BR^2(X \to Y\gamma)$ are derived for the case of stable and invisible Y. These limits apply to single and pair production of excited neutrinos ($X = \nu^*, Y = \nu$), to neutralino production ($X = \tilde{\chi}_2^0, Y = \tilde{\chi}_1^0$) and to supersymmetric models in which $X = \tilde{\chi}_1^0$ and $Y = \tilde{G}$ is a light gravitino. The case of macroscopic decay lengths of particle X is considered for $e^+e^- \to XX$, $X \to Y\gamma$, when $M_Y \approx 0$. The single-photon results are also used to place upper limits on superlight gravitino pair production as well as graviton-photon production in the context of theories with additional space dimensions.

The OPAL Collaboration

G. Abbiendi[2], K. Ackerstaff[8], C. Ainsley[5], P.F. Akesson[3], G. Alexander[22], J. Allison[16],
K.J. Anderson[9], S. Arcelli[17], S. Asai[23], S.F. Ashby[1], D. Axen[27], G. Azuelos[18,a], I. Bailey[26], A.H. Ball[8],
E. Barberio[8], R.J. Barlow[16], J.R. Batley[5], S. Baumann[3], T. Behnke[25], K.W. Bell[20], G. Bella[22],
A. Bellerive[9], S. Bentvelsen[8], S. Bethke[14,i], O. Biebel[14,i], I.J. Bloodworth[1], P. Bock[11], J. Böhme[14,h],
O. Boeriu[10], D. Bonacorsi[2], M. Boutemeur[31], S. Braibant[8], P. Bright-Thomas[1], L. Brigliadori[2],
R.M. Brown[20], H.J. Burckhart[8], J. Cammin[3], P. Capiluppi[2], R.K. Carnegie[6], A.A. Carter[13],
J.R. Carter[5], C.Y. Chang[17], D.G. Charlton[1,b], C. Ciocca[2], P.E.L. Clarke[15], E. Clay[15], I. Cohen[22],
O.C. Cooke[8], J. Couchman[15], C. Couyoumtzelis[13], R.L. Coxe[9], M. Cuffiani[2], S. Dado[21],
G.M. Dallavalle[2], S. Dallison[16], R. Davis[28], A. de Roeck[8], P. Dervan[15], K. Desch[25], B. Dienes[30,h],
M.S. Dixit[7], M. Donkers[6], J. Dubbert[31], E. Duchovni[24], G. Duckeck[31], I.P. Duerdoth[16],
P.G. Estabrooks[6], E. Etzion[22], F. Fabbri[2], M. Fanti[2], A.A. Faust[28], L. Feld[10], P. Ferrari[12], F. Fiedler[8],
I. Fleck[10], M. Ford[5], A. Frey[8], A. Fürtjes[8], D.I. Futyan[16], P. Gagnon[12], J.W. Gary[4], G. Gaycken[25],
C. Geich-Gimbel[3], G. Giacomelli[2], P. Giacomelli[8], D.M. Gingrich[28,a], D. Glenzinski[9], J. Goldberg[21],
C. Grandi[2], K. Graham[26], E. Gross[24], J. Grunhaus[22], M. Gruwé[25], P.O. Günther[3], C. Hajdu[29]
G.G. Hanson[12], M. Hansroul[8], M. Hapke[13], K. Harder[25], A. Harel[21], C.K. Hargrove[7], M. Harin-Dirac[4],
A. Hauke[3], M. Hauschild[8], C.M. Hawkes[1], R. Hawkings[25], R.J. Hemingway[6], C. Hensel[25], G. Herten[10],
R.D. Heuer[25], M.D. Hildreth[8], J.C. Hill[5], P.R. Hobson[25], A. Hocker[9], K. Hoffman[8], R.J. Homer[1],
A.K. Honma[8], D. Horváth[29,c], K.R. Hossain[28], R. Howard[27], P. Hüntemeyer[25], P. Igo-Kemenes[11],
D.C. Imrie[25], K. Ishii[23], F.R. Jacob[20], A. Jawahery[17], H. Jeremie[18], C.R. Jones[5], P. Jovanovic[1],
T.R. Junk[6], N. Kanaya[23], J. Kanzaki[23], G. Karapetian[18], D. Karlen[6], V. Kartvelishvili[16],
K. Kawagoe[23], T. Kawamoto[23], P.I. Kayal[28], R.K. Keeler[26], R.G. Kellogg[17], B.W. Kennedy[20],
D.H. Kim[19], K. Klein[11], A. Klier[24], T. Kobayashi[23], M. Kobel[3], T.P. Kokott[3], S. Komamiya[23],
R.V. Kowalewski[26], T. Kress[4], P. Krieger[6], J. von Krogh[11], T. Kuhl[3], M. Kupper[24], P. Kyberd[13],
G.D. Lafferty[16], H. Landsman[21], D. Lanske[14], I. Lawson[26], J.G. Layter[4], A. Leins[31], D. Lellouch[24],
J. Letts[12], L. Levinson[24], R. Liebisch[11], J. Lillich[10], B. List[8], C. Littlewood[5], A.W. Lloyd[1],
S.L. Lloyd[13], F.K. Loebinger[16], G.D. Long[26], M.J. Losty[7], J. Lu[27], J. Ludwig[10], A. Macchiolo[18],
A. Macpherson[28], W. Mader[3], M. Mannelli[8], S. Marcellini[2], T.E. Marchant[16], A.J. Martin[13],
J.P. Martin[18], G. Martinez[17], T. Mashimo[23], P. Mättig[24], W.J. McDonald[28], J. McKenna[27],
T.J. McMahon[1], R.A. McPherson[26], F. Meijers[8], P. Mendez-Lorenzo[31], F.S. Merritt[9], H. Mes[7],
A. Michelini[2], S. Mihara[23], G. Mikenberg[24], D.J. Miller[15], W. Mohr[10], A. Montanari[2], T. Mori[23],
K. Nagai[8], I. Nakamura[23], H.A. Neal[12,f], R. Nisius[8], S.W. O'Neale[1], F.G. Oakham[7], F. Odorici[2],
H.O. Ogren[12], A. Oh[8], A. Okpara[11], M.J. Oreglia[9], S. Orito[23], G. Pásztor[8,j], J.R. Pater[16],
G.N. Patrick[20], J. Patt[10], P. Pfeifenschneider[14], J.E. Pilcher[9], J. Pinfold[28], D.E. Plane[8], B. Poli[2],
J. Polok[8], O. Pooth[8], M. Przybycień[8,d], A. Quadt[8], C. Rembser[8], H. Rick[4], S.A. Robins[21],
N. Rodning[28], J.M. Roney[26], S. Rosati[3], K. Roscoe[16], A.M. Rossi[2], Y. Rozen[21], K. Runge[10],
O. Runolfsson[8], D.R. Rust[12], K. Sachs[6], T. Saeki[23], O. Sahr[31], W.M. Sang[25], E.K.G. Sarkisyan[22],
C. Sbarra[26], A.D. Schaile[31], O. Schaile[31], P. Scharff-Hansen[8], S. Schmitt[11], M. Schröder[8],
M. Schumacher[25], C. Schwick[8], W.G. Scott[20], R. Seuster[14,h], T.G. Shears[8], B.C. Shen[4],
C.H. Shepherd-Themistocleous[5], P. Sherwood[15], G.P. Siroli[2], A. Skuja[17], A.M. Smith[8], G.A. Snow[17],
R. Sobie[26], S. Söldner-Rembold[10,e], S. Spagnolo[20], M. Sproston[20], A. Stahl[3], K. Stephens[16], K. Stoll[10],
D. Strom[19], R. Ströhmer[31], B. Surrow[8], S.D. Talbot[1], S. Tarem[21], R.J. Taylor[15], R. Teuscher[9],
M. Thiergen[10], J. Thomas[15], M.A. Thomson[8], E. Torrence[9], S. Towers[6], T. Trefzger[31], I. Trigger[8],
Z. Trócsányi[30,g], E. Tsur[22], M.F. Turner-Watson[1], I. Ueda[23], P. Vannerem[10], M. Verzocchi[8], H. Voss[8],
J. Vossebeld[8], D. Waller[6], C.P. Ward[5], D.R. Ward[5], P.M. Watkins[1], A.T. Watson[1], N.K. Watson[1],
P.S. Wells[8], T. Wengler[8], N. Wermes[3], D. Wetterling[11] J.S. White[6], G.W. Wilson[16], J.A. Wilson[1],
T.R. Wyatt[16], S. Yamashita[23], V. Zacek[18], D. Zer-Zion[8]

[1]School of Physics and Astronomy, University of Birmingham, Birmingham B15 2TT, UK

[2]Dipartimento di Fisica dell' Università di Bologna and INFN, I-40126 Bologna, Italy

[3]Physikalisches Institut, Universität Bonn, D-53115 Bonn, Germany

[4]Department of Physics, University of California, Riverside CA 92521, USA

[5]Cavendish Laboratory, Cambridge CB3 0HE, UK

[6]Ottawa-Carleton Institute for Physics, Department of Physics, Carleton University, Ottawa, Ontario K1S 5B6, Canada

[7]Centre for Research in Particle Physics, Carleton University, Ottawa, Ontario K1S 5B6, Canada

[8]CERN, European Organisation for Nuclear Research, CH-1211 Geneva 23, Switzerland

[9]Enrico Fermi Institute and Department of Physics, University of Chicago, Chicago IL 60637, USA

[10]Fakultät für Physik, Albert Ludwigs Universität, D-79104 Freiburg, Germany

[11]Physikalisches Institut, Universität Heidelberg, D-69120 Heidelberg, Germany

[12]Indiana University, Department of Physics, Swain Hall West 117, Bloomington IN 47405, USA

[13]Queen Mary and Westfield College, University of London, London E1 4NS, UK

[14]Technische Hochschule Aachen, III Physikalisches Institut, Sommerfeldstrasse 26-28, D-52056 Aachen, Germany

[15]University College London, London WC1E 6BT, UK

[16]Department of Physics, Schuster Laboratory, The University, Manchester M13 9PL, UK

[17]Department of Physics, University of Maryland, College Park, MD 20742, USA

[18]Laboratoire de Physique Nucléaire, Université de Montréal, Montréal, Quebec H3C 3J7, Canada

[19]University of Oregon, Department of Physics, Eugene OR 97403, USA

[20]CLRC Rutherford Appleton Laboratory, Chilton, Didcot, Oxfordshire OX11 0QX, UK

[21]Department of Physics, Technion-Israel Institute of Technology, Haifa 32000, Israel

[22]Department of Physics and Astronomy, Tel Aviv University, Tel Aviv 69978, Israel

[23]International Centre for Elementary Particle Physics and Department of Physics, University of Tokyo, Tokyo 113-0033, and Kobe University, Kobe 657-8501, Japan

[24]Particle Physics Department, Weizmann Institute of Science, Rehovot 76100, Israel

[25]Universität Hamburg/DESY, II Institut für Experimental Physik, Notkestrasse 85, D-22607 Hamburg, Germany

[26]University of Victoria, Department of Physics, P O Box 3055, Victoria BC V8W 3P6, Canada

[27]University of British Columbia, Department of Physics, Vancouver BC V6T 1Z1, Canada

[28]University of Alberta, Department of Physics, Edmonton AB T6G 2J1, Canada

[29]Research Institute for Particle and Nuclear Physics, H-1525 Budapest, P O Box 49, Hungary

[30]Institute of Nuclear Research, H-4001 Debrecen, P O Box 51, Hungary

[31]Ludwigs-Maximilians-Universität München, Sektion Physik, Am Coulombwall 1, D-85748 Garching, Germany

[a] and at TRIUMF, Vancouver, Canada V6T 2A3

[b] and Royal Society University Research Fellow

[c] and Institute of Nuclear Research, Debrecen, Hungary

[d] and University of Mining and Metallurgy, Cracow

[e] and Heisenberg Fellow

[f] now at Yale University, Dept of Physics, New Haven, USA

[g] and Department of Experimental Physics, Lajos Kossuth University, Debrecen, Hungary

[h] and MPI München

[i] now at MPI für Physik, 80805 München

[j] and Research Institute for Particle and Nuclear Physics, Budapest, Hungary.

1   Introduction

We describe measurements and searches using a data sample of photonic events with large missing energy collected in 1998 with the OPAL detector at LEP. The events result from e^+e^- collisions at a centre-of-mass energy of 188.6 GeV with an integrated luminosity of 177.3 pb^{-1}. The present paper builds on publications from earlier data samples at lower centre-of-mass energies [1, 2]. This data-set at 189 GeV gives discovery potential in a new kinematic regime with about a four-fold increase in integrated luminosity. Measurements of photonic event production have also been made by the other LEP collaborations at centre-of-mass energies above the W pair threshold [3], including new results from L3 and DELPHI at $\sqrt{s} = 189$ GeV [4].

The single-photon and acoplanar-photons search topologies presented here are designed to select events with one or more photons and significant missing transverse energy, indicating the presence of at least one neutrino-like invisible particle which interacts only weakly with matter. The event selections for these search topologies are similar to those used in our recent publication [1]. The single-photon search topology is sensitive to events in which there are one or two photons and missing energy which, within the Standard Model, are expected from the $e^+e^- \to \nu\overline{\nu}\gamma(\gamma)$ process[1]. The acoplanar-photons search topology is designed to select events with two or more photons and significant missing transverse energy which, within the Standard Model, are expected from the $e^+e^- \to \nu\overline{\nu}\gamma\gamma(\gamma)$ process.

The single photon topology provides a direct measurement of the invisible width of the Z^0 and can probe charged and neutral triple gauge couplings. The acoplanar-photons topology can probe $WW\gamma\gamma$ quartic couplings in the $e^+e^- \to \nu_e\overline{\nu_e}\gamma\gamma$ process. The neutral and quartic gauge coupling measurements will be described in forthcoming papers based on the event selections described herein.

These photonic final-state topologies are sensitive to several different new physics scenarios. A generic classification is $e^+e^- \to XY$ or $e^+e^- \to XX$ where X is neutral and can decay radiatively $(X \to Y\gamma)$ and Y is stable and only weakly interacting. For the general case of massive X and Y this includes conventional supersymmetric processes $(X = \tilde{\chi}_2^0, Y = \tilde{\chi}_1^0)$. These topologies also have particularly good sensitivity for the special case of $M_Y \approx 0$. This applies both to the production of excited neutrinos $(X = \nu^*, Y = \nu)$ and to supersymmetric models in which the lightest supersymmetric particle (LSP) is a light gravitino and $\tilde{\chi}_1^0$ is the next-to-lightest supersymmetric particle (NLSP) which decays to a gravitino and a photon $(X = \tilde{\chi}_1^0, Y = \tilde{G})$. The neutralino life-time in such models is a free parameter and so we also address the possibility of neutralino-pair production with macroscopic decay lengths. One type of new physics which could be seen in the single-photon topology is the production of an invisible particle in association with a photon. An example of this is graviton-photon production, $e^+e^- \to G\gamma$ [5, 6]. This can occur within string theory models which allow gravitons to propagate in a higher-dimensional space but restrict Standard Model particles to the usual four space-time dimensions [7]. Another type of new physics is the production of invisible particles tagged by initial-state radiation. One example[2] is production of a pair of gravitinos, $e^+e^- \to \tilde{G}\tilde{G}\gamma$, as in the superlight gravitino model [8]. The acoplanar-photons search topology also has sensitivity to the production of two particles, one invisible, or with an invisible decay mode, and the other decaying into two photons.

This paper will first describe the OPAL detector and the Monte Carlo samples used. A brief summary of the event selections will then be given, followed by cross-section measurements for $e^+e^- \to \nu\overline{\nu}\gamma(\gamma)$ and $e^+e^- \to \nu\overline{\nu}\gamma\gamma(\gamma)$ and comparisons with Standard Model expectations. The new physics search results will then be discussed.

---

[1]The photon in parentheses denotes that the presence of this photon is allowed but not required.

[2]The initial-state radiation diagram is one of many that contribute to this final state.

2 Detector and Monte Carlo Samples

The OPAL detector, which is described in detail in [9], contains a silicon micro-vertex detector surrounded by a pressurized central tracking system operating inside a solenoid with a magnetic field of 0.435 T. The region outside the solenoid (barrel) and the pressure bell (endcap) is instrumented with scintillation counters, presamplers and the lead-glass electromagnetic calorimeter (ECAL). The magnet return yoke is instrumented for hadron calorimetry and is surrounded by external muon chambers. Electromagnetic calorimeters close to the beam axis measure luminosity and complete the acceptance.

The measurements presented here are mainly based on the observation of clusters of energy deposited in the lead-glass electromagnetic calorimeter. This consists of an array of 9,440 lead-glass blocks in the barrel ($|\cos\theta| < 0.82$) with a quasi-pointing geometry and two dome-shaped endcap arrays, each of 1,132 lead-glass blocks, covering the polar angle[3] range ($0.81 < |\cos\theta| < 0.984$). Fully hermetic electromagnetic calorimeter coverage is achieved beyond the end of the ECAL down to small polar angles with the use of the the gamma-catcher calorimeter, the forward calorimeter (FD) and the silicon-tungsten calorimeter (SW).

Scintillators in the barrel and endcap regions are used to reject backgrounds from cosmic ray interactions by providing time measurements for the large fraction ($\approx 80\%$) of photons which convert in the material in front of the ECAL. The barrel time-of-flight (TOF) scintillator bars are located outside the solenoid in front of the barrel ECAL and match its geometrical acceptance ($|\cos\theta| < 0.82$). Tile endcap (TE) scintillator arrays [10] are located at $0.81 < |\cos\theta| < 0.955$ behind the pressure bell and in front of the endcap ECAL.

The integrated luminosities of the data samples are determined to better than 1% from small-angle Bhabha scattering events in the SW calorimeter. Triggers [11] based on electromagnetic energy deposits in either the barrel or endcap electromagnetic calorimeters lead to full trigger efficiency for photonic events passing the event selection criteria described in the following section.

The KORALZ [12] and NUNUGPV98 [13] Monte Carlo generators were used to simulate the expected Standard Model signal process, $e^+e^- \to \nu\overline{\nu} +$ photon(s). For other expected Standard Model processes, a number of different generators were used: RADCOR [14] for $e^+e^- \to \gamma\gamma(\gamma)$; BHWIDE [15] for $e^+e^- \to e^+e^-$; TEEGG [16] for $e^+e^- \to e^+e^-\gamma$; KORALW [17] using `grc4f` [18] matrix elements for $e^+e^- \to \ell^+\ell^-\nu\overline{\nu}(\gamma)$ and $e^+e^- \to \nu\overline{\nu}q\overline{q}$, and KORALZ for $e^+e^- \to \mu^+\mu^-(\gamma)$ and $e^+e^- \to \tau^+\tau^-(\gamma)$. The Vermaseren program [19] and `grc4f` were used for $e^+e^- \to e^+e^-\ell^+\ell^-$. The expected contributions from each of these Standard Model processes were evaluated using a total equivalent integrated luminosity at least five times larger than the integrated luminosity of the data sample.

To simulate possible new physics processes of the type $e^+e^- \to XY$ and $e^+e^- \to XX$ where X decays to $Y\gamma$ and Y escapes detection, a modified version of the SUSYGEN [20] Monte Carlo generator was used to produce neutralino pair events of the type $e^+e^- \to \tilde{\chi}_2^0\tilde{\chi}_1^0$ and $e^+e^- \to \tilde{\chi}_2^0\tilde{\chi}_2^0$, $\tilde{\chi}_2^0 \to \tilde{\chi}_1^0\gamma$, with isotropic angular distributions for the production and decay of $\tilde{\chi}_2^0$ and including initial-state radiation. Monte Carlo events were generated at 48 (for XY production) and 42 (for XX production) points in the kinematically accessible region of the (M_X, M_Y) plane. A Monte Carlo generator was written to simulate the superlight gravitino signature $\tilde{G}\tilde{G}\gamma$, discussed in Section 5.1.4. The KORALZ $\nu\overline{\nu}\gamma(\gamma)$ sample was used to determine the efficiency for graviton-photon production in the context of additional space dimensions, by means of an event reweighting (see section 5.1.5). The

---

[3]In the OPAL coordinate system, θ is the polar angle defined with respect to the electron beam direction and ϕ is the azimuthal angle.

same procedure was also used to calculate the efficiency for $\tilde{G}\tilde{G}\gamma$ production, and compared with the prediction of the direct Monte Carlo simulation. All the Monte Carlo samples described above were processed through the OPAL detector simulation [21].

Simulation of $e^+e^- \rightarrow XX$, $X \rightarrow Y\gamma$ signal events with $M_Y \approx 0$ where M_X has a finite non-zero lifetime τ_X was implemented in the full simulation of the OPAL detector. In particular, the massive quasi-stable neutral particle X was assigned properties similar to a heavy neutrino for the purpose of propagation, and then propagated within the GEANT [22] framework, according to its initial kinematics and τ_X before forcing the $X \rightarrow Y\gamma$ decay.

3   Photonic Event Selection

This section summarizes the criteria for selecting single-photon and acoplanar-photons events. The kinematic acceptance of each selection is defined in terms of the photon energy, E_γ, and the photon polar angle, θ. In addition, the scaled energy, x_γ, is defined as E_γ/E_{beam}, and the scaled transverse energy, x_T, as $x_\gamma \sin\theta$.

Single-Photon - One or two photons accompanied by invisible particle(s):

- At least one photon with $x_T > 0.05$ and with $15° < \theta < 165°$ ($|\cos\theta| < 0.966$).

Acoplanar-Photons - Two or more photons accompanied by invisible particle(s):

- At least two photons, each with $x_\gamma > 0.05$ and $15° < \theta < 165°$, or one photon with $E_\gamma > 1.75$ GeV and $|\cos\theta| < 0.8$ and a second photon with $E_\gamma > 1.75$ GeV and $15° < \theta < 165°$.
- The transverse momentum $p_T^{\gamma\gamma}$ of the two-photon system consisting of the two highest energy photons must satisfy $p_T^{\gamma\gamma}/E_{\text{beam}} > 0.05$.

In each of the two cases we retain acceptance for events with additional photons in which the resulting photonic system is still consistent with the presence of significant missing energy. This reduces the sensitivity of each measurement to the modelling of higher-order contributions. Consequently, a large fraction of the kinematic acceptance of the acoplanar-photons selection is also contained in the kinematic acceptance of the single-photon selection.

3.1   Single-Photon Event Selection

The single-photon selection criteria are explained in detail in a previous publication [1]. After defining the kinematic acceptance, additional cuts on cluster quality, forward energy, muon chamber and hadron calorimeter information, and multiphoton kinematics are used to remove cosmic ray backgrounds, beam related backgrounds and standard model physics backgrounds that have no missing energy. Then events are classed as either having or not having photon conversion candidates based on tracking chamber information. Each of these two classes has somewhat different additional selection criteria based on charged track activity, time-of-flight information, and other background suppression cuts.

Several improvements have been made to the single-photon selection used in this analysis compared with the previous analysis [1]. They are described in detail in Appendix A.

3.2 Acoplanar-Photons Event Selection

The acoplanar-photons selection has classes of selection requirements similar to those of the single-photon selection. The details of the acoplanar-photons selection are described in our previous analysis [1]; changes with respect to the previous analysis are minimal and are given in Appendix A.

The requirement of a second photon in an event reduces many of the backgrounds which are otherwise a problem for the single-photon analysis. For this reason, the acoplanar photons selection can tolerate a lower energy threshold for the most energetic photon, as well as looser but more inclusive acceptance requirements for photon conversions. On the other hand, the single-photon selection has more acceptance for events having no time-of-flight information for the photons. In order to obtain the best overall acceptance for acoplanar-photons, we have added to the acoplanar-photons selection that part of the single-photon selection which contains two photons within the kinematic acceptance of the acoplanar-photons selection. This addition results in a relative increase in efficiency of 9.6% for Standard Model $e^+e^- \to \nu\overline{\nu}\gamma\gamma(\gamma)$ events.

4 Selection Results

The results of the single-photon and acoplanar-photons selections and the corresponding cross-section measurements and other measured event quantities are given below in sections 4.1 and 4.2. Results from both selections are summarized in Table 1.

4.1 Single-Photon

After applying the single-photon selection criteria to the data sample, 643 events are selected. The expected contribution from cosmic ray and beam-related backgrounds is 4.6 ± 1.5 events. These backgrounds have been estimated from events having out-of-time TOF or TE information, but passing all other selection criteria, and from events selected with looser criteria that have been visually scanned. Of the expected physics backgrounds from plausible sources, $e^+e^- \to e^+e^-\gamma$, $e^+e^- \to \ell^+\ell^-\nu\overline{\nu}(\gamma)$, $e^+e^- \to e^+e^-\ell^+\ell^-$, $e^+e^- \to \nu\overline{\nu}q\overline{q}$, $e^+e^- \to \mu^+\mu^-\gamma$ and $e^+e^- \to \tau^+\tau^-\gamma$ have non-negligible contributions[4]. The total number of expected physics background events is 4.6 ± 0.5 and the contributing sources are summarized in Table 2. The number of events expected from the Standard Model process $e^+e^- \to \nu\overline{\nu}\gamma(\gamma)$ as predicted by KORALZ is 679 ± 5 (stat) ± 14 (sys) where the systematic error is from experimental sources as discussed later. The number of events observed is consistent with the number expected from $e^+e^- \to \nu\overline{\nu}\gamma(\gamma)$ plus the background. The efficiency for selecting $e^+e^- \to \nu\overline{\nu}\gamma(\gamma)$ events within the kinematic acceptance of the single-photon selection is $(82.1 \pm 1.7)\%$. For both the single-photon and acoplanar-photons selections, efficiency losses due to vetoes on random detector occupancy range from about $(3\text{-}5)\%$. Quoted efficiencies include these losses. The single-photon cross-section for $\sqrt{s} = 189$ GeV, accounting for detector and selection efficiencies and subtracting the estimated background, is 4.35 ± 0.17 (stat) ± 0.09 (sys) pb.

The systematic error on the cross-section measurement from knowledge of the efficiency and normalisation is estimated to be 2.1%. The contributing uncertainties are summarized in Table 3. The dominant systematics are the selection efficiency uncertainty (1.5%) and the uncertainty on the detector occupancy estimate (1%). The event selection efficiency is controlled using a data sample of

---

[4] The expected number of events from the Standard Model process $e^+e^- \to \nu\overline{\nu}\nu\overline{\nu}\gamma(\gamma)$ is negligible and is neglected in both the efficiency and background estimates

around 1200 $e^+e^- \to \gamma\gamma$ events. In particular, the efficiency and time response of the TB and TE scintillators are measured from these data and small correction factors applied to the efficiency. The selection efficiency systematic includes the uncertainties on such corrections and an estimate of the residual uncertainty on the efficiency. The occupancy, estimated from random beam-crossing triggers, is typically 4% and we assign an error of 1%. We have compared the estimated efficiency using the NUNUGPV98 and KORALZ event generators. We find that the relative efficiency difference is $(0.5 \pm 0.4)\%$ and assign an error of 0.5% to take into account the sensitivity to the modelling of the photon energy, angle and multiplicity distributions. This source of error is considerably reduced from our previous publications, largely because both generators that are now used are designed to model accurately $\nu\bar{\nu}\gamma\gamma$ events. Additional systematic errors on the efficiency arise from uncertainties in modelling the material close to or inside the beam-pipe which accounts for photons which convert early (20% relative uncertainty) and from systematic effects in the track reconstruction and parameter estimation which affect the association of tracks to ECAL clusters. Uncertainties in the photon energy scale, resolution and angular measurement give small additional systematic contributions.

The cross-section as a function of centre-of-mass energy is plotted in Figure 1. Cross-section results from the current analysis and from our earlier publications [1, 2] are plotted. The curve shows the predicted cross-section from the KORALZ event generator for the Standard Model process $e^+e^- \to \nu\bar{\nu}\gamma(\gamma)$. The data are consistent with the prediction.

Figure 2a shows the recoil mass distribution, where the recoil mass $M_{\rm recoil}$ is defined as the mass recoiling against the photon (or against the two-photon system). The peak in the distribution at $M_{\rm Z}$ is due to a large contribution from the decay $Z^0 \to \nu\bar{\nu}$. Figure 2b shows the polar angle distribution along with the $e^+e^- \to \nu\bar{\nu}\gamma(\gamma)$ Monte Carlo expectation. In both distributions, there is consistency between data and Monte Carlo, although we note a deficit in the radiative return peak and a slight excess in the low energy, high recoil mass region.

The single-photon selection is designed to allow for the presence of a second photon in order to accept events from the $e^+e^- \to \nu\bar{\nu}\gamma\gamma$ process. Thirty-six observed events are considered to be two-photon events (i.e. have a second photon with deposited energy exceeding 300 MeV and with $15° < \theta < 165°$), consistent with the expectation of 33.6 ± 1.5 events from the KORALZ Monte Carlo. Of these, 20 fall within the kinematic acceptance of the acoplanar photon selection, as compared to the KORALZ expectation of 23.5 ± 1.0.

4.2   Acoplanar-Photons

The acoplanar-photons selection applied to the data sample yields 24 events, in good agreement with the KORALZ prediction of 26.9 ± 1.2 events for the Standard Model $e^+e^- \to \nu\bar{\nu}\gamma\gamma(\gamma)$ contribution. The expected contribution from other Standard Model processes and from cosmic ray and beam related backgrounds is 0.11 ± 0.04 events. The selection efficiency for $e^+e^- \to \nu\bar{\nu}\gamma\gamma(\gamma)$ events within the kinematic acceptance of the selection is $(66.4 \pm 2.9)\%$. The corresponding cross-section is 0.204 ± 0.043 pb, compared to a KORALZ prediction of 0.228 ± 0.002 pb. The OPAL measurements of the cross-sections at $\sqrt{s} = 130, 136, 161, 172, 183$ and 189 GeV are summarized in Table 4. Results for $\sqrt{s} < 189$ GeV have been taken from our previous publications [1, 2].

The dominant source of systematic uncertainties is modelling of the reconstruction efficiency, especially the simulation of the detector material and consequent photon conversion probabilities. Other sources arise from uncertainties on the electromagnetic calorimeter energy scale and resolution, on the integrated luminosity measurement, on detector occupancy estimates and from comparisons of

different Monte Carlo event generators for the process $e^+e^- \to \nu\bar{\nu}\gamma\gamma(\gamma)$. The relative systematic error from all sources is 4.3%.

The kinematic properties of the selected events are displayed in Figure 3 where they are compared with the predicted distributions for $e^+e^- \to \nu\bar{\nu}\gamma\gamma(\gamma)$ obtained using the KORALZ generator normalized to the integrated luminosity of the data. Plot (a) shows the recoil mass distribution of the selected acoplanar-photon pairs (or of the two most-energetic photons in the case of events with three or more photons). The distribution is peaked near the mass of the Z^0 as is expected for contributions from $e^+e^- \to \nu\bar{\nu}\gamma\gamma(\gamma)$. The resolution of the recoil mass is typically 3-5 GeV for $M_{\mathrm{recoil}} \approx M_{\mathrm{Z}}$. Plot (b) shows the distribution of the scaled energy of the second most energetic photon. Plot (c) shows the $\gamma\gamma$ invariant-mass distribution for which the mass resolution is typically 0.7-1.9 GeV. Plot (d) shows the distribution in scaled transverse momentum of the selected two-photon system. There is 1 selected event having a third photon with deposited energy above 300 MeV and within the polar-angle acceptance of the selection. The corresponding expectation from KORALZ is 1.20 ± 0.08 events.

5   Data Interpretation

The results of the single-photon and acoplanar-photons selections are used to test the Standard Model and search for new physics contributions.

For the XY and XX searches, we test the range of the following product branching ratios which are consistent with the data: $\sigma(e^+e^- \to XY) \cdot \mathrm{BR}(X \to Y\gamma)$ and $\sigma(e^+e^- \to XX) \cdot \mathrm{BR}^2(X \to Y\gamma)$. Given lack of evidence for signal, we then set 95% CL upper limits on these quantities. This is done both for the general case of massive X and Y, and also separately for the special case of $M_{\mathrm{Y}} \approx 0$. All efficiencies are first evaluated under the assumption that the decay length of X is zero. For the XX search in the special case of $M_{\mathrm{Y}} \approx 0$, we evaluate the efficiency as a function of the non-zero lifetime of the X particle, thus quantifying the sensitivity of the search for the general case of non-prompt decay. For both the XY and XX searches, Monte Carlo samples were generated for a variety of mass points in the kinematically accessible region of the $(M_{\mathrm{X}}, M_{\mathrm{Y}})$ plane. To set limits for arbitrary M_{X} and M_{Y}, the efficiency over the entire $(M_{\mathrm{X}}, M_{\mathrm{Y}})$ plane is parameterized using the efficiencies calculated at the generated mass points. As justified previously [1], we restrict the searches to $M_{\mathrm{X}} + M_{\mathrm{Y}} > M_{\mathrm{Z}}$ for the single-photon topology and to M_{X} values larger than about $M_{\mathrm{Z}}/2$ for the acoplanar-photons topology.

5.1   Single-Photon

With the single-photon topology we measure the number of light neutrino species and observe a rise in the cross-section at low photon energies which is consistent with the additional cross-section expected from charged current contributions to $e^+e^- \to \nu_e\overline{\nu_e}\gamma(\gamma)$. We also give results of searches for XY production, superlight gravitino pair production, and graviton-photon production in the context of models with extra space dimensions.

5.1.1   Neutrino Counting

Single-photon events are expected within the Standard Model from the process $e^+e^- \to \nu\bar{\nu}\gamma(\gamma)$. At the tree level, the cross-section for muon-type and tau-type neutrinos is attributable solely to s-channel Z production with initial-state radiation. For electron-type neutrinos, the single photon cross-section

arises from Feynman diagrams corresponding to s-channel Z production with initial-state radiation and t-channel W exchange with radiation from the initial-state or the exchanged W. Higher order electroweak processes such as WW boxes are expected to give a negligible contribution to the cross-section.

The results of the single-photon selection are used to measure the size of the s-channel Z production contributions and the W-related contributions (W amplitude squared plus the W-Z interference), which we parameterize in terms of N_ν and f_W. The measurement of the pure s-channel Z production contributions is a direct measurement of the Z invisible width, which is related to the effective number of light neutrino generations, N_ν, defined as the ratio of the Z invisible width to the expected width in the Standard Model for one neutrino generation. The W-related contributions are parameterized by a multiplicative scale factor, f_W, defined to be 1 for the Standard Model expectation.

In order to measure N_ν and/or f_W, we perform a binned fit to both the overall event rate and to the shape of the photon energy distribution by minimising the negative log-likelihood:

$$- \log L = - \log \mathcal{P}(n_{exp}(E_\gamma, N_\nu, f_W) \to n_{obs}(E_\gamma)) \tag{1}$$

where n_{exp} is given by

$$n_{exp}(E_\gamma, N_\nu, f_W) = f_W \, n_{exp}^W(E_\gamma) + N_\nu \, n_{exp}^Z(E_\gamma). \tag{2}$$

Here n_{obs} is the observed number of events, n_{exp} is the expected number of events as a function of N_ν and f_W derived by reweighting fully simulated $\nu\bar{\nu}\gamma(\gamma)$ events, and $\mathcal{P}$ represents the Poisson probability for observing n_{obs} events given an expectation of n_{exp}. n_{exp}^W is the number of events for Standard Model W contributions[5] and n_{exp}^Z is the number of s-channel events expected per neutrino generation; both n_{exp}^W and n_{exp}^Z were evaluated using the NUNUGPV98 generator[6].

The dominant systematic errors arise from the uncertainty on the selection efficiency and from the theoretical uncertainty on the expected number of events, with a minor contribution from the limited Monte Carlo statistics. The relative uncertainty on the selection efficiency is 2.1% and was discussed in Section 4. We assign a value of 2% to the theoretical uncertainty based on comparisons and estimated precisions of the NUNUGPV98, KORALZ and grc$\nu\nu\gamma$ [23] event generators. In addition, an uncertainty related to the modelling of the photon energy spectrum is assigned, again estimated by comparing the NUNUGPV98 and KORALZ event generators. Other sources of systematic error, such as the uncertainty on the centre-of-mass energy and the expected background, result in negligible contributions.

In a first step, we check the consistency with the Standard Model predictions by fitting for both N_ν and f_W. The results are $f_W = 1.12 \pm 0.13$ (stat) ± 0.12 (sys) and $N_\nu = 2.63 \pm 0.15$ (stat) ± 0.11 (sys) with a correlation coefficient of -41%. Figure 4 shows the 70%, 95% and 99% probability contours in the space of the two parameters, while Figure 5 shows the photon energy distribution for the events selected at 189 GeV, compared to the expectation with $f_W = 1.12$, $N_\nu = 2.63$. The data are seen to be in fair agreement with the Standard Model prediction for $N_\nu = 3$ and $f_W = 1$. In particular, the W contributions are observed with a high degree of significance, even when allowing N_ν to be unconstrained.

In a second step, we assume the W contributions to be as predicted by the Standard Model and fit for N_ν. The result is:

$$N_\nu = 2.69 \pm 0.13 \text{ (stat)} \pm 0.11 \text{ (sys)}. \tag{3}$$

---

[5]Both the pure W t-channel, which is dominant, and its interference with the Z^0 s-channel are taken into account assuming Standard Model couplings of electrons and electron-type neutrinos.

[6] Using the NUNUGPV98 feature which allows $\nu_e\bar{\nu}_e\gamma(\gamma)$ and $\nu_\mu\bar{\nu}_\mu\gamma(\gamma)$ events to be generated separately

Alternatively, one can assume $N_\nu = 3$ as indicated by the precise, but less direct, measurements of the Z lineshape [24], and fit for the relative size of the W-contributions. The result is $f_W = 0.99 \pm 0.11$ (stat) ± 0.12 (sys), establishing that the W-contributions are observed and are consistent with the expectations from the Standard Model.

5.1.2 Search for $e^+e^- \to XY$, $X \to Y\gamma$; General case: $M_Y \geq 0$

We search for evidence of new physics processes of type $e^+e^- \to XY$, $X \to Y\gamma$. To select candidate new physics events, kinematic-consistency and degraded-resolution cuts are applied to events in the single-photon event sample. The kinematic-consistency cuts require that the energy of the most energetic photon be within the range kinematically consistent with mass values (M_X, M_Y) after accounting for energy resolution effects. The degraded-resolution cuts reject events in which the most energetic photon is in the angular regions $0.78 < |\cos\theta| < 0.82$ or $|\cos\theta| > 0.95$; energy resolution is significantly degraded in these regions and the Monte Carlo simulation is less reliable. These cuts are approximately 94% efficient in selecting signal events within the kinematic acceptance of the single-photon selection, assuming uniform energy and $\cos\theta$ signal distributions.

Two methods are used to search for, and place upper limits on, contributions from $e^+e^- \to XY$, $X \to Y\gamma$. The first is an event-counting method, based simply on the total number of events selected as candidates. The kinematic cuts, described above, are sufficiently loose that the results are relatively insensitive to the shapes of signal distributions in photon energy or $\cos\theta$ that result from the specifics of a particular model. Thus this method gives the more generally applicable cross-section limits for XY production. In many models, however, the distributions for the production and decay angles in the process $e^+e^- \to XY$, $X \to Y\gamma$ are approximately isotropic. We therefore also perform a likelihood-based analysis to search for new physics contributions under the assumption of isotropically distributed production and decay angles. This results in a substantial increase in experimental sensitivity, since energy and angular distributions can now be used to differentiate signal from background.

In both methods, Standard Model background is assumed to be from $e^+e^- \to \nu\overline{\nu}\gamma(\gamma)$ only. Background from other sources, including the estimated cosmic ray and beam-related background, is small and is neglected in the limit calculations. Since uncertainties due to energy scale and resolution effects in the low $M_X - M_Y$ region lead to large relative uncertainties in the estimated efficiencies, we restrict our search to the region in which $M_X - M_Y > 5$ GeV.

Event-Counting Method:
Upper limits are calculated based on the total numbers of observed and expected background events using the method described in reference [25]. This procedure is similar to the method used in our previous publication [1], with the exception that only the kinematic-consistency and degraded-resolution cuts are applied in order to improve the generality of the results.

The total signal efficiency within the single-photon kinematic acceptance is approximately 85%, varying by less than 1% over most of the (M_X, M_Y) plane. However, the efficiency decreases significantly when the mass difference $M_X - M_Y$ becomes small, due to low photon energies resulting from the $X \to Y\gamma$ decay. Contributions to the systematic error on the efficiency for selecting events from potential new physics sources are similar in nature and size to those discussed in our previous publication. The total relative systematic error varies from 2.5 to 5.5%, depending on M_X and M_Y. These systematic errors have been treated according to the method in reference [26]; the effect on the upper limits is small. Uncertainties in the $\nu\overline{\nu}\gamma(\gamma)$ background estimate have a more significant

10

effect on the upper limits, and are treated by means of a convolution within the limit calculations. A relative 3% uncertainty has been assigned to the expected background contribution, based on factors considered in the cross-section measurement and assigning a 2% theoretical uncertainty.

There are 552 events selected after the degraded-resolution cuts are applied; the KORALZ expectation is 601 ± 14. The photon energy distribution for these events is shown in Figure 6. The number of selected events after further application of the kinematic-consistency cuts depends on the values for M_X and M_Y; ranges for observed and expected events are displayed as contour plots in Figure 7. The consistency between the number of observed events (n_{obs}) and the number of expected background events (n_b) is given in Figure 8. Plotted is P_{fluct}, the probability for observing at least n_{obs} events given a background expectation of $n_b \pm \sigma_b$ events, defined by:

$$P_{\text{fluct}} = \sum_{n=n_{obs}}^{\infty} \left[\int_{-\infty}^{\infty} d\mu \left(\frac{e^{(n_b - \mu)^2 / 2\sigma_b^2}}{\sqrt{2\pi\sigma_b^2}} \right) \cdot \left(e^{-\mu} \frac{\mu^n}{n!} \right) \right]. \tag{4}$$

This figure is intended to highlight regions in the (M_X, M_Y) plane with an excess of events that could potentially be indicative of new physics. Such an excess would appear as a very low probability ($P_{\text{fluct}} \ll 1\%$). However, a deficit of events is actually observed for most of the (M_X, M_Y) plane. This leads to high values for P_{fluct}; for example, for $n_{obs} \gg 1$, a value $P_{\text{fluct}} = 0.97$ indicates a deficit consistent at approximately the 3% level. The calculated values of P_{fluct} range from 0.71% to 99.94%.

Values with rather low and high probability occur partly because we consider several thousand points in the (M_X, M_Y) plane; each of these has a different set of kinematic-consistency cuts which select different parts of the photon energy spectrum. The net effect is that almost every possible energy range is selected for some (M_X, M_Y) value. For example, as seen in Figure 6, there is a deficit in the energy range from approximately 26 to 38 GeV; this range corresponds roughly to $M_X = 113$ GeV and $M_Y = 74$ GeV.

The general structure of Figure 8 can also be understood from the photon energy spectrum. There is an overall deficit of approximately 49 events ($\sim 1.7\sigma$). As seen in Figure 6, most of the deficit lies in the region of the radiative return peak, while there is an excess in the low-energy region. For regions in the (M_X, M_Y) plane for which low-energy photons are not kinematically allowed, events populating the low-energy region of the energy spectrum are rejected and the significance of the remaining deficit is enhanced. In particular, this occurs when $M_X - M_Y$ is relatively large, and accounts for the large P_{fluct} values in the low-M_Y region of Figure 8. Conversely, regions with a small mass difference $M_X - M_Y$ correspond to low photon energies, which in turn correspond to the region of the photon energy spectrum in which there is an excess. This accounts for the small P_{fluct} values in the low $M_X - M_Y$ region of Figure 8.

Cross-section times branching-ratio upper limits calculated using the event-counting method are shown in Figure 9 and range from 43 to 409 fb. Results for one M_X, M_Y pair ($M_X = 125, M_Y = 63$ GeV) are shown as an addition to the expected $\nu\bar{\nu}\gamma(\gamma)$ background in Figure 6. The added signal contribution is that which would be expected from a cross-section equal to the 95% CL upper limit.

Likelihood Method:

The likelihood-based analysis is a straightforward extension of an extended maximum likelihood fit [27]. Upper limits are calculated using information from the photon energy and angular distributions as well as the total number of observed events. The number of observed events, number of expected background events, and signal efficiencies are the same as in the event-counting method.

The likelihood function is given by

$$L(\sigma_s) = \mathcal{P}((n_b + n_s) \to n_{obs}) \cdot \prod_i [f_b P_b(E_i, \theta_i) + f_s P_s(E_i, \theta_i)] \tag{5}$$

where the product is over all selected events in the data, and

- n_b = expected number of background events,

- $n_s = \epsilon_s \sigma_s \mathcal{L}$ = expected number of signal events, with ϵ_s the efficiency for observing signal events, σ_s the signal cross-section times branching ratio, and $\mathcal{L}$ the integrated luminosity,

- n_{obs} = number of candidate events observed in the data,

- $\mathcal{P}((n_b + n_s) \to n_{obs}) = e^{-(n_b+n_s)}(n_b + n_s)^{n_{obs}}/n_{obs}!$ = the Poisson probability to observe n_{obs} events given an expectation of $(n_b + n_s)$,

- $P_{b,s}(E_i, \theta_i)$ = probability density (normalized to one) for a photon i resulting from a background (b) or signal (s) process to have an energy E_i and polar angle θ_i, and

- $f_{b,s} = n_{b,s}/(n_b + n_s)$ = relative fraction of background or signal events.

The expected number of background events, n_b, is determined from a Monte Carlo sample of events generated by KORALZ. The signal efficiency, ϵ_s, is calculated by integrating an energy and angular distribution function over the region of kinematic acceptance (including kinematic-consistency and degraded-resolution cuts), and scaling the result to account for additional efficiency losses due to other cuts in the single-photon selection. This energy and angular distribution function serves as the the signal probability density function $P_s(E, \theta)$. The background probability density function $P_b(E, \theta)$ is obtained from a parameterization of the distributions formed by simulated $\nu\bar{\nu}\gamma(\gamma)$ events generated by KORALZ and NUNUGPV98. In the region $|\cos\theta| < 0.72$, the photon energy and angular distributions are independent, with the angular distribution given by $1/\sin^2\theta$ and the energy distribution determined with a parameterization. In the region $|\cos\theta| > 0.72$, energy resolution is dependent on $\cos\theta$. In this region, energy distributions are parameterized separately for slices of width 0.1 in $|\cos\theta|$; when properly normalized, these parameterizations together form the 2-dimensional probability distribution.

The value for σ_s is not fixed; it is instead treated as a free parameter in the likelihood function. When properly normalized, the likelihood function can be thought of as a probability density function for a hypothesized σ_s consistent with the observed data. Restricting σ_s to be non-negative, the 95% CL upper limit σ^{95} is therefore determined from the following equation:

$$0.95 = \frac{\displaystyle\int_0^{\sigma^{95}} L(\sigma_s)d\sigma_s}{\displaystyle\int_0^{\infty} L(\sigma_s)d\sigma_s}. \tag{6}$$

The validity of the likelihood-based method was tested with Monte Carlo simulations. Two types of test were performed. The first test relies on the following definition of a 95% CL limit: if the true signal cross-section happened to be equal to the 95% CL limit, then at least 95% of a large number of identical experiments would result in data that are more signal-like (as defined by a likelihood comparison) than the experiment from which the 95% CL likelihood was derived. This type of test was performed for various combinations of large and small numbers of expected signal and background

events, using events generated randomly according to distributions derived from the expected XY signal and $\nu\overline{\nu}\gamma(\gamma)$ background. The second type of test involved the calculation of a large number of 95% CL upper limits from samples generated with an identical signal cross-section. In this case, at least 95% of the calculated upper limits should be larger than the actual signal cross-section. Both types of test yielded agreement with expectations to within statistical errors (typically less than 0.5%). In addition, tests with fully simulated Monte Carlo events were used to test for any biases due to the signal and background parameterizations. No significant biases were found.

Sources of systematic errors are the same as for the event-counting method, and are treated in the same manner. However, when calculating limits using the likelihood method, an additional 4% relative uncertainty in experimental sensitivity has been added to account for effects due to uncertainties in the background and signal parameterizations. The 4% estimate is the result of tests using different parameterizations; the uncertainty is again treated according to the method given in reference [26].

The 95% CL upper limits resulting from the likelihood method are shown as a function of M_X and M_Y in Figure 10. The values range from 23 fb to 371 fb.

5.1.3   Search for $e^+e^- \rightarrow XY$, $X \rightarrow Y\gamma$; Special case: $M_Y \approx 0$

The case $M_Y \approx 0$ is applicable to excited neutrino models and to some supersymmetric models mentioned earlier. The results presented above include this case and no separate analysis is performed, although the results are highlighted here. The upper limits on $\sigma(e^+e^- \rightarrow XY) \cdot BR(X \rightarrow Y\gamma)$ for $M_Y \approx 0$ as a function of M_X range from 23 to 107 fb using the likelihood method, and from 43 to 170 fb using the event-counting method. The limits are shown in Figure 11 for both methods. Also shown is the average limit expected in the absence of signal for the event-counting method. The actual limit is significantly lower than the expected limit (see discussion in Section 5.1.2). Table 5 gives more details of the search results.

5.1.4   Gravitino Pair Production

A supersymmetric model has been proposed in which the gravitino is very light [8]. This model predicts a new source of single-photon events from the process $e^+e^- \rightarrow \tilde{G}\tilde{G}\gamma$. We use the single-photon topology to place constraints on the cross-section and therefore the gravitino mass in this model. The differential cross-section is given by

$$\frac{d^2\sigma}{dx_\gamma \, d\cos\theta} = \left(\frac{\alpha G_N^2}{45}\right) \frac{s^3}{m_{\tilde{G}}^4} f_{\tilde{G}\tilde{G}\gamma}(x_\gamma, \cos\theta) \tag{7}$$

where α is the fine structure constant, G_N is the gravitational constant, $m_{\tilde{G}}$ is the gravitino mass, x_γ is the photon scaled energy (E_γ/E_{beam}) and θ is the polar angle, with

$$f_{\tilde{G}\tilde{G}\gamma}(x, \cos\theta) = 2(1-x)^2 \left[\frac{(1-x)(2-2x+x^2)}{x\sin^2\theta} + \frac{x(-6+6x+x^2)}{16} - \frac{x^3\sin^2\theta}{32}\right], \tag{8}$$

leading to a soft photon energy spectrum.

Two methods were used to determine the efficiency for observing events from $e^+e^- \rightarrow \tilde{G}\tilde{G}\gamma$. The first is by reweighting simulated $\nu\overline{\nu}\gamma(\gamma)$ events generated by KORALZ. Each simulated event is weighted by $f_{\tilde{G}\tilde{G}\gamma}(x, \cos\theta)/f_{KZ}(x, \cos\theta)$, where f_{KZ} is the 2-dimensional energy and angular distribution for the most energetic photon in events generated by KORALZ. We use a parameterization

f_{KZ} which is valid up to photon energies of about 60 GeV, and thus we establish a kinematic acceptance region for $\tilde{G}\tilde{G}\gamma$ production: $x_T > 0.05$, $15° < \theta < 165°$, and $E_\gamma < 60$ GeV. We note that the cross-section for $\tilde{G}\tilde{G}\gamma$ production with photon energies above 60 GeV is negligible.

In addition, a Monte Carlo generator was written to generate events according to the distribution given in Equation 8. Initial state radiation was treated in a manner identical to that used by the EXOTIC [28] generator. Efficiencies were calculated and found to be identical to those using the reweighting method to within statistical errors.

To achieve maximum sensitivity[7], we place a maximum energy requirement on the observed photon energy: $E_\gamma < 30$ GeV. With this requirement, we observe 195 candidates with an expected $\nu\bar{\nu}\gamma$ background of 179.6 ± 5.4. The efficiency within the above kinematic acceptance region is estimated by the Monte Carlo to be 82.8%, and was assigned a relative 5% uncertainty. Using the event-counting method described earlier, we place a 95% CL cross-section upper limit of 293 fb, giving a lower limit[8] on the gravitino mass of 8.7 μeV.

5.1.5 Graviton-Photon: Search for Extra Space Dimensions

There has been recent interest in string theory models which postulate the existence of additional compactified space dimensions; these models allow gravitons to propagate freely in the higher-dimensional space while restricting Standard Model particles to a 3+1 dimensional hypersurface [7]. The fundamental mass scale in this class of theories, M_D, governs the rate of graviton production; it is possible that direct graviton-photon production could occur at significant rates at LEP2 energies with an experimental signature of a single photon with missing energy [5,6]. The single-photon search topology can therefore be used to place constraints on the fundamental mass scale M_D (or, equivalently, on the size of the extra dimensions) by placing limits on the graviton-photon cross-section.

The differential cross-section is given by

$$\frac{d^2\sigma}{dx_\gamma \, d\cos\theta} = \frac{\alpha S_{\delta-1}}{64 M_D{}^2} \left(\frac{\sqrt{s}}{M_D}\right)^\delta f_{G\gamma}(x_\gamma, \cos\theta) \tag{9}$$

where δ is the number of extra dimensions and $S_{\delta-1}$ is the surface area of a δ-dimensional sphere of unit radius, with

$$f_{G\gamma}(x, \cos\theta) = \frac{2(1-x)^{\frac{\delta}{2}-1}}{x(1-\cos^2\theta)} \left[(2-x)^2(1-x+x^2) - 3x^2\cos^2\theta(1-x) - x^4\cos^4\theta\right]. \tag{10}$$

We use the event-counting method to place limits on graviton-photon production in the cases $2 \le \delta \le 7$. We use the same kinematic acceptance region as described in Section 5.1.4: $x_T > 0.05$, $E_\gamma < 60$ GeV, and $15° < \theta < 165°$. The expected photon energy spectrum is soft, so in order to improve sensitivity, we require observed photon energies to be less than 34 GeV for all values of δ.

The efficiency for observing events from $e^+e^- \to G\gamma$ is determined by reweighting simulated $\nu\bar{\nu}\gamma(\gamma)$ events generated by KORALZ in a manner equivalent to that described in Section 5.1.4: simulated

---

[7] The optimization condition chosen was that the expected upper limit on the cross-section for contributions from the $e^+e^- \to \tilde{G}\tilde{G}\gamma$ signal process be minimised, where the expected upper limit is defined as the average limit one would expect to set in the absence of signal.

[8] Evaluated with $\alpha = \frac{1}{128}$

events are weighted by $f_{G\gamma}(x, \cos\theta)/f_{KZ}(x, \cos\theta)$, where f_{KZ} is the same KORALZ parameterization used earlier. The distributions f_{KZ} and $f_{G\gamma}$ have roughly similar shapes, and the calculated efficiency is insensitive to small differences in the KORALZ parameterization.

We observe 208 candidates with an expected $\nu\bar{\nu}\gamma$ contribution of 196.0 ± 5.9 events. Assuming a 5% relative uncertainty in the signal efficiency, upper limits on the cross-section and corresponding lower limits on M_D for $2 \leq \delta \leq 7$ have been calculated[9]. The results are given in Table 6 based on the convention[10] of Equation 2 in reference [5].

5.2 Acoplanar-Photons

5.2.1 Search for $e^+e^- \rightarrow XX$, $X \rightarrow Y\gamma$; General case: $M_Y \geq 0$

The searches for $e^+e^- \rightarrow XX$, $X \rightarrow Y\gamma$, both for the general case discussed here and the special case of $M_Y \approx 0$ discussed in 5.2.2, use the methods described in our previous publication [1]. Selected events are classified as consistent with a given value of M_X and M_Y if the energy of each of the photons falls within the region kinematically accessible to photons from the process $e^+e^- \rightarrow XX$, $X \rightarrow Y\gamma$, including resolution effects. The selection efficiencies at each generated grid point for the $e^+e^- \rightarrow XX$, $X \rightarrow Y\gamma$ Monte Carlo events are shown in Table 7. These values include the efficiency of the kinematic consistency requirement which is higher than 95% at each generated point in the (M_X, M_Y) plane for which $M_X - M_Y > 5$ GeV. Events from $e^+e^- \rightarrow \nu\bar{\nu}\gamma\gamma(\gamma)$ are typically characterized by a high-energy photon from the radiative return to the Z^0 and a second lower energy photon. The kinematic consistency requirement is such that the two photons must have energies within the same (kinematically accessible) region. As M_X and M_Y increase, the allowed range of energy for the photons narrows, and fewer $\nu\bar{\nu}\gamma\gamma(\gamma)$ events will be accepted. For the 24 selected events, the distribution of the number of events consistent with a given mass point (M_X, M_Y) is consistent with the expectation from $e^+e^- \rightarrow \nu\bar{\nu}\gamma\gamma(\gamma)$ Monte Carlo, over the full (M_X, M_Y) plane.

In our previous publication, because of concerns about the modelling of the Standard Model process $e^+e^- \rightarrow \nu\bar{\nu}\gamma\gamma(\gamma)$, all limits derived from the acoplanar photons analysis were obtained without accounting for the expected background. The theoretical situation is now greatly improved, with two event generators [12,13] agreeing to better than 1% for the total cross-section for this process within the kinematic acceptance of this analysis. For that reason, in this paper, all limits derived from this selection have been calculated taking the (KORALZ) background estimate into account. Figure 12 shows the 95% CL exclusion regions for $\sigma(e^+e^- \rightarrow XX) \cdot BR^2(X \rightarrow Y\gamma)$. The limits vary from 33 fb to 103 fb for $M_X > 45$ GeV and $M_X - M_Y > 5$ GeV. In the region 2.5 GeV $\leq M_X - M_Y < 5.0$ GeV, the efficiency falls off rapidly (see Table 7). As this rapid fall increases the associated uncertainty in the efficiency, no limits have been set in this region.

Systematic errors are due primarily to limited Monte Carlo statistics at the generated (M_X, M_Y) points and the uncertainty on the efficiency parameterization across the (M_X, M_Y) plane. The combined relative uncertainty on the efficiency varies from about (3-6)% across the plane (for $M_X - M_Y > 5$ GeV). All systematic uncertainties are accounted for in the manner advocated in reference [26]. This also applies to the limits for the $M_Y \approx 0$ case, presented in the next section.

---

[9]Evaluated also with $\alpha = \frac{1}{128}$

[10]The convention of reference [6] differs.

5.2.2 Search for $e^+e^- \to XX$, $X \to Y\gamma$; Special case: $M_Y \approx 0$

For the special case of $M_Y \approx 0$ the kinematic consistency requirements differ from those used for the general case. One can calculate [29] the maximum mass, $M_X^{\max}$, which is consistent with the measured three-momenta of the two photons, assuming a massless Y. A cut on $M_X^{\max}$ provides further suppression of the $\nu\overline{\nu}\gamma\gamma(\gamma)$ background while retaining high efficiency for the signal hypothesis. This is discussed in more detail in reference [2]. We require that the maximum kinematically allowed mass be greater than $M_X - 5$ GeV, which retains $(95.5^{+2.0}_{-1.0})\%$ relative efficiency for signal at all values of M_X while suppressing much of the remaining $\nu\overline{\nu}\gamma\gamma(\gamma)$ background. In our previous publication we also applied a recoil-mass cut at 80 GeV. In the case where background is not accounted for in the limit calculation, such a cut improves the expected sensitivity of the analysis. With background subtraction this is no longer the case. Therefore that cut has been removed.

Figure 13 shows the expected $M_X^{\max}$ distribution for signal Monte Carlo events with $M_X = 90$ GeV and for $e^+e^- \to \nu\overline{\nu}\gamma\gamma(\gamma)$ Monte Carlo events. Also shown is the distribution of the selected data events. For the $M_Y \approx 0$ case, the efficiencies calculated from Monte Carlo events are shown in Table 8 after application of the event selection criteria and then after the cut on $M_X^{\max}$. Also shown in Table 8 are the number of selected events consistent with each value of M_X as well as the expected number of events from $e^+e^- \to \nu\overline{\nu}\gamma\gamma(\gamma)$. The number of selected events consistent with a given value of M_X varies from 14, for $M_X \geq 45$ GeV, to 3 events at the kinematic limit. The expected number of events decreases from 15.8 ± 0.7 at $M_X \geq 45$ GeV to 1.34 ± 0.07 consistent with $M_X \geq 94$ GeV.

Based on the efficiencies and the number of selected events, we calculate a 95% CL upper limit on $\sigma(e^+e^- \to XX) \cdot \mathrm{BR}^2(X \to Y\gamma)$ for $M_Y \approx 0$ as a function of M_X. This is shown as the solid line in Figure 14. The limit is between 50 and 80 fb for M_X values from 45 GeV up to the kinematic limit. Also shown as a dashed line is the expected limit, defined as the average limit one would expect to set in the absence of signal. The limits can be used to set model-dependent limits on the mass of the lightest neutralino in supersymmetric models in which the NLSP is the lightest neutralino and the LSP is a light gravitino ($X = \tilde{\chi}_1^0, Y = \tilde{G}$). Shown in Figure 14 as a dotted line is the (Born-level) cross-section prediction from a specific light gravitino LSP model [30] in which the neutralino composition is purely bino, with $m_{\tilde{e}_R} = 1.35 m_{\tilde{\chi}_1^0}$ and $m_{\tilde{e}_L} = 2.7 m_{\tilde{\chi}_1^0}$. Within the framework of this model, $\tilde{\chi}_1^0$ masses between 45 and 88.3 GeV are excluded at 95% CL.

As described in section 2, the efficiencies over the full angular range have been calculated using isotropic angular distributions for production and decay of X. The validity of this model has been examined based on the angular distributions calculated for photino pair production in reference [31]. For models proposed in reference [32], the production angular distributions are more central and so this procedure is conservative. For a $1 + \cos^2 \theta$ production angular distribution expected for t-channel exchange of a very heavy particle according to reference [31], the relative efficiency reduction would be less than 2% at all points in the (M_X, M_Y) plane.

5.2.3 Search for $e^+e^- \to XX$, $X \to Y\gamma$; Special case: $M_Y \approx 0$ and macroscopic decay length

As an extension to the special case of $M_Y \approx 0$, we consider the sensitivity of the acoplanar-photons search to $e^+e^- \to XX$, $X \to Y\gamma$ when X has a macroscopic decay length. This extension evaluates the selection efficiency using signal Monte Carlo samples with various lifetime values τ_X. The $X \to Y\gamma$ decay is treated by a modified OPAL detector simulation package designed to handle delayed decays (as described in section 2). The range of lifetimes considered extends from the near-zero lifetime value

of $\tau_X = 10^{-15}$ s to $\tau_X = 10^{-7}$ s at which point $c\tau$ is 30 m. Such long lifetimes lead to decays outside the sensitive volume of the OPAL detector (determined by the outer radius of the ECAL), which implies a natural cutoff in sensitivity.

As with the zero lifetime case, the $(M_X^{\mathrm{max}} > M_X - 5 \ \mathrm{GeV})$ requirement is applied. The relative efficiency of this cut decreases with increasing lifetime, but exceeds 90% for all (M_X, τ_X) combinations with high (greater than 50%) selection efficiencies. For (M_X, τ_X) combinations with lower selection efficiencies, the relative efficiency falls more rapidly with increasing τ_X, but does not drop below 60% for the (M_X, τ_X) combinations considered. The loss in relative efficiency of the M_X^{max} cut is expected due to the definition of M_X^{max}, but the cut is maintained to allow comparison between the prompt decay and macroscopic decay length selection efficiencies. The resulting selection efficiencies for macroscopic decay lengths are given in Table 9. Also listed in Table 9 are the number of events observed in the data and the expected $\mathrm{e^+e^-} \to \nu\bar{\nu}\gamma\gamma(\gamma)$ background. The efficiencies indicate that sensitivity to macroscopic decay lengths is maintained up to lifetimes of 10^{-9} s but falls rapidly for longer lifetimes. This is as expected, since for $\tau_X = 10^{-9}$ s the decay length ranges from 30 to 3 cm for the values of M_X considered, so that the $X \to Y\gamma$ decays typically occur well within the confines of the detector. For lifetimes greater than 10^{-9} s, the decrease in efficiency is two-fold. The primary loss is due to the increased decay length, implying fewer $X \to Y\gamma$ decays within the sensitive detector volume. Selection efficiency is also lost with increasing τ_X since larger lifetimes result in a delayed arrival time of the photon at the ECAL, which, if sufficiently late, causes the event to be vetoed due to the timing cuts imposed by the analysis. The effect of the event kinematics is also seen in the increase in selection efficiency for a given lifetime as M_X approaches its threshold value, corresponding to a drop in β from 0.84 at M_X=50 GeV to 0.10 at M_X=94 GeV.

Contributions to the systematic error in the selection efficiency are (in order of significance) the limited Monte Carlo statistics, the efficiency parameterisation in the (M_X, τ_X) plane and the modelling of the timing cuts. The total contributions are given in Table 9.

Given the efficiencies and the number of selected events, the 95% CL upper limit on $\sigma(\mathrm{e^+e^-} \to XX)\cdot\mathrm{BR}^2(X \to Y\gamma)$ for $M_Y \approx 0$ as a function of M_X and τ_X is calculated, and is shown in figure 15. The background-subtracted limits from the prompt decay analysis are used to define the profile as a function of M_X for $\tau_X = 10^{-15}$ s. The interpolation of the limit to larger lifetimes is done by factoring the selection efficiencies of Table 9 into the 95% confidence level limits on $\sigma(\mathrm{e^+e^-} \to XX) \cdot \mathrm{BR}^2(X \to Y\gamma)$ for $M_Y \approx 0$. As in Section 5.2.2 the Born-level cross-section of the neutralino NLSP Gravitino LSP model of [30] is used to give an exclusion region in the (neutralino mass, lifetime) plane. This exclusion region is superimposed on Figure 15 and gives the excluded domain in the (M_X, τ_X) plane within the same specific light gravitino LSP model [30] discussed above.

6   Conclusions

We have searched for photonic events with large missing energy in two topologies in data taken with the OPAL detector at LEP, at a centre-of-mass energy of 189 GeV.

In the single-photon selection, which requires at least one photon with $x_T > 0.05$ in the region $15° < \theta < 165°$ ($|\cos\theta| < 0.966$), 643 events are observed in the data. The background-subtracted cross-section measurement of 4.35 ± 0.17 (stat) ± 0.09 (sys) pb is consistent with the KORALZ prediction of 4.66 pb from the Standard Model $\nu\bar{\nu}\gamma(\gamma)$ process. Interpreting the results as a measurement of the effective number of light neutrino species, we measure $\mathrm{N}_\nu = 2.69 \pm 0.13(\mathrm{stat}) \pm 0.11(\mathrm{sys})$. We also observe significant W contributions to the cross-section with a rate consistent with the Standard

Model expectation.

We calculate upper limits on the cross-section times branching ratio for the process $e^+e^- \to XY$, $X \to Y\gamma$ using two methods: an event-counting method, which is insensitive to energy or angular distribution shapes and is therefore relatively model-independent, and a likelihood method, which assumes isotropic production and decay angular distributions and has greater sensitivity. In the region of interest in the (M_X, M_Y) plane, the limits vary from 43 to 409 fb using the event-counting method and from 23 to 371 fb using the likelihood method. These limits include the special case of $M_Y \approx 0$, where the limit varies between 43 and 170 fb using the event-counting method and from 23 to 107 fb using the likelihood method. We note that some of these limits are much more stringent than would be expected on average in the absence of signal contributions.

We set a 95% CL cross-section upper limit on $e^+e^- \to \tilde{G}\tilde{G}\gamma$ production of 293 fb implying a lower limit on the gravitino mass of 8.7 μeV in the superlight gravitino model of reference [8]. In the context of string theory models with extra space dimensions, upper limits on the cross-section for graviton-photon production of between 309 and 271 fb at 95% CL are set, giving lower limits on the fundamental mass scale varying between 1086 and 470 GeV for between 2 and 7 additional dimensions respectively.

The acoplanar-photons selection requires at least two photons with scaled energy $x_\gamma > 0.05$ within the polar angle region $15° < \theta < 165°$ or at least two photons with energy $E_\gamma > 1.75$ GeV with one satisfying $|\cos\theta| < 0.8$ and the other satisfying $15° < \theta < 165°$. In each case, the requirement $p_T^{\gamma\gamma}/E_{\text{beam}} > 0.05$ is also applied. There are 24 events selected. The KORALZ prediction for the contribution from $e^+e^- \to \nu\bar{\nu}\gamma\gamma(\gamma)$ is 26.9 ± 1.2 events; contribution from other sources is 0.11 events. The number of events observed in the data and their kinematic distributions are consistent with Standard Model expectations. We derive 95% CL upper limits on $\sigma(e^+e^- \to XX) \cdot BR^2(X \to Y\gamma)$ ranging from 33 to 103 fb for the general case of massive X and Y. For the special case of $M_Y \approx 0$, the 95% CL upper limits on $\sigma(e^+e^- \to XX) \cdot BR^2(X \to Y\gamma)$ range from 50 to 80 fb. For the case of macroscopic decay lengths, these values range from 50 fb at short lifetimes to 8.8 pb for lifetimes as long as 10^{-7} s.

The results of the acoplanar-photons search are used to place model-dependent lower limits on the $\tilde{\chi}_1^0$ mass in a specific light gravitino LSP model [30]. Masses between 45 and 88.3 GeV are excluded at 95% CL for promptly decaying neutralinos, while for a $\tilde{\chi}_1^0$ lifetime of 10^{-8} s ($c\tau = 3$m), masses between 45 and 81 GeV are excluded.

Appendix

A Improvements to Event Selections

Detailed descriptions of the event selection criteria are given in a previous publication [1]. This appendix describes changes and updates to the selections used in the present publication.

A.1 Single-Photon Selection

There have been several improvements to the single-photon selection:

- Non-conversion candidates in the endcap region ($|\cos\theta| > 0.82$) are no longer required to have a good in-time associated TE hit, although candidates with associated out-of-time TE hits are still rejected. This change reduces sensitivity to the modelling of the material between the interaction point and the TE scintillators, and results in a relative increase in efficiency of about 19% in the endcap region with an associated increase in cosmic and beam-related background of about 1.3 events. The special background vetos continue to be applied to all non-conversion candidates in the endcap regardless of the presence of TE timing.

- The cluster extent cut has been modified for events in the endcap region. This cut had been fixed at lower centre-of-mass energies and was no longer fully efficient at $\sqrt{s} = 189$ GeV, particularly for beam energy photons. Events with the primary photon candidate in the region $|\cos\theta| > 0.82$ are now rejected if $\Delta\phi \cdot \sin^{1.46}\theta / \ln E_\gamma > 0.05$ radians[11], where $\Delta\phi$ is the ϕ extent of the cluster and E_γ is the cluster energy in GeV. The result is a relative increase in efficiency of about 13% in the endcap region with no significant change in expected cosmic and beam-related background.

- Small changes have been made to the timing requirements. The timing cuts for the photon candidates with TOF associated hits ($|\cos\theta| < 0.82$) have been relaxed for certain periods of data-taking, resulting in an efficiency increase of 2.3% for events with a photon in $|\cos\theta| < 0.82$ with a TOF associated hit. The expected cosmic ray background increases by about 10%.

  In addition, the majority of events rejected by poorly measured TOF times are recovered. In cases where the ECAL cluster and the TOF z-measurement from time difference differ by more than 40 cm, modified arrival times based on the ECAL cluster position and the time measurement at each end of the scintillator are constructed. Events are retained if either modified arrival time is within 5 ns of the expected time for a photon originating from the interaction point. As a result, the probability for a signal event to be rejected due to bad TOF timing falls from 0.6% to less than 0.1% with no measurable change in the cosmic and beam-related background.

- The efficiency of the photon conversion consistency criteria has been improved substantially. In particular, all reconstructed tracks in the event (usually two for signal events) are now used to test association of a charged track to an ECAL cluster, and the association test also considers the disfavoured solution of the jet-chamber left-right ambiguity to account for cases where the incorrect solution has been chosen.

---

[11] The $\sin\theta$ dependence was parameterized for beam energy photons using samples of real and simulated $e^+e^- \to \gamma\gamma$ events.

- Improved redundancy in the rejection of beam-related backgrounds for conversion candidates with $x_T < 0.1$ and $|\cos\theta| > 0.90$ is introduced, based on the measured z-difference of the track's point of closest approach to the interaction point.

- An additional beam-halo veto was implemented; events are rejected if ECAL clusters exceeding 100 MeV in deposited energy are found within 20 cm in the $r - \phi$ plane but on opposite ends of the ECAL endcap. This veto provides better rejection of beam-halo background and has negligible effect on signal efficiencies.

- A minor addition was made to the special background vetoes used for non-conversion candidates. Events are now explicitly rejected if there is a large amount of hadronic energy in an HCAL cluster associated with the ECAL cluster of the primary photon candidate. This provides better redundancy with existing cuts in terms of background rejection, with negligible inefficiency even for beam energy photons.

A.2 Acoplanar-Photons Selection

The acoplanar-photons selection is almost identical to that described in our previous publication. The only difference involves the timing requirements for candidates with associated TOF hits. These were relaxed for certain periods of the data-taking in the same manner as described above for the single-photon selection.

Acknowledgements

References

[1] OPAL Collab., G. Abbiendi et al., Eur. Phys. J. **C8** (1999) 23.

[2] OPAL Collab., K. Ackerstaff et al., Eur. Phys. J. **C2** (1998) 607.

[3] ALEPH Collab., R. Barate et al., Phys. Lett. **B420** (1998)127;
DELPHI Collab., P. Abreu et al., Eur. Phys. J. **C1** (1998) 1;
L3 Collab., M. Acciarri et al., Phys. Lett. **B415** (1997) 299;
ALEPH Collab., R. Barate et al., Phys. Lett. **B429** (1998) 201.

[4] L3 Collab., M. Acciarri et al., Phys. Lett. **B472** (2000) 420;
DELPHI Collab., P. Abreu et al., CERN-EP/2000-021, submitted to Eur. Phys. J. **C**.

[5] G.F. Giudice, R. Rattazzi and J.D. Wells, Nucl. Phys. **B544** (1999) 3

[6] E.A. Mirabelli, M. Perelstein and M.E. Peskin, Phys. Rev. Lett. **82** (1999) 2236.

[7] N. Arkani-Hamed, S. Dimopoulos and G. Dvali, Phys. Lett. **B429** (1998) 263;
I. Antoniadis, N. Arkani-Hamed, S. Dimopoulos and G. Dvali, Phys. Lett. **B436** (1998) 257;
N. Arkani-Hamed, S. Dimopoulos and G. Dvali, hep-ph/9807344.

[8] A. Brignole, F. Feruglio and F. Zwirner, Nucl. Phys. **B516** (1998) 13 and Erratum : Nucl. Phys. **B555** (1999) 653.

[9] OPAL Collab., K. Ahmet et al., Nucl. Instrum. Methods **A305** (1991) 275;
S. Anderson et al., Nucl. Instrum. Methods **A403** (1998) 326;
B.E. Anderson et al., IEEE Transactions on Nuclear Science **41** (1994) 845.

[10] G. Aguillion et al., Nucl. Instrum. Methods **A417** (1998) 266.

[11] M. Arignon et al., Nucl. Instrum. Methods **A313** (1992) 103.

[12] S. Jadach, B.F.L. Ward and Z. Wąs, Comp. Phys. Comm. **79** (1994) 503.
Version 4.02 was used including a recommended correction to the NDIST0 subroutine.

[13] G. Montagna, M. Moretti, O. Nicrosini and F. Piccinini, Nucl. Phys. **B541** (1999) 31.

[14] F.A. Berends and R. Kleiss, Nucl. Phys. **B186** (1981) 22.

[15] S. Jadach, W. Placzek and B.F.L. Ward, Phys. Lett. **B390** (1997) 298.

[16] D. Karlen, Nucl. Phys. **B289** (1987) 23.

[17] S. Jadach et al., KORALW1.42, CERN-TH/98-242.

[18] J. Fujimoto et al., Comp. Phys. Comm. **100** (1997) 128.

[19] J. A. M. Vermaseren, Nucl. Phys. **B229** (1983) 347. R. Bhattacharya, J. Smith, G. Grammer,
Phys. Rev. D **15** (1977) 3267;
J. Smith, J. A. M. Vermaseren and G. Grammer, Phys. Rev. D **15** (1977) 3280.

[20] S. Katsanevas and S. Melachronios, CERN/96-01, Vol.2 (1996) 328.

[21] J. Allison et al., Nucl. Instrum. Methods **A317** (1992) 47.

[22] R. Brun et al., GEANT 3, Report DD/EE/84-1, CERN (1989).

[23] Y. Kurihara et al., hep-ph/9908422

[24] The LEP Collaborations, CERN-EP/99-015.

[25] Particle Data Group, R.M. Barnett et al., Phys. Rev. **D54** (1996) 1.

[26] R.D. Cousins and V.L. Highland, Nucl. Instrum. Methods **A320** (1992) 331.

[27] See for example L. Lyons, *Statistics for Nuclear and Particle Physicists*, Cambridge University Press, Cambridge (1986).

[28] R. Tafirout and G. Azuelos, accepted by Comp. Phys. Comm.

[29] J.L. Lopez and D.V. Nanopoulos, Mod. Phys. Lett. **A11** (1996) 2473;
Phys. Rev. **D55** (1997) 4450.

[30] C.Y. Chang and G.A. Snow, UMD/PP/97-57;
K. S. Babu, C. Kolda and F. Wilczek, Phys. Rev. Lett. **77** (1996) 3070.

[31] J. Ellis and J.S. Hagelin, Phys. Lett. **B122** (1983) 303.

[32] S. Dimopoulos et al., Phys. Rev. Lett. **76** (1996) 3494;
D.R. Stump, M. Wiest, C.P. Yuan, Phys. Rev. **D54** (1996) 1936;
S. Ambrosanio et al., Phys. Rev. **D54** (1996) 5395.

Quantity	Topology	
	Single-photon	Acoplanar photons
N_{obs}	643	24
$N_{expected}$	$679 \pm 5 \pm 14$	26.9 ± 1.2
N_{bkg}	9.2 ± 1.6	0.11 ± 0.04
Efficiency (%)	82.1 ± 1.7	66.4 ± 2.9
$\sigma_{meas}(pb)$	$4.35 \pm 0.17 \pm 0.09$	0.204 ± 0.043
$\sigma_{KORALZ}(pb)$	4.66 ± 0.03 (stat)	0.228 ± 0.002 (stat)

Table 1: Summary of results for the single and acoplanar photons selections. Shown are the number of events observed in the data; the number of expected $e^+e^- \to \nu\overline{\nu}\gamma(\gamma)$ (single-photon) or $e^+e^- \to \nu\overline{\nu}\gamma\gamma(\gamma)$ (acoplanar-photons) events based on the KORALZ event generator; the number of events expected from backgrounds; the selection efficiency within the kinematic acceptance of the selections (defined in section 3); the background-subtracted, measured cross-section within the kinematic acceptance; and the expected cross-section based on the KORALZ generator. Errors when not marked are statistical and systematic added in quadrature. When two errors are shown, the first is statistical and the second is systematic.

Background process	Number of events
$e^+e^- \to e^+e^-\gamma$	0.3 ± 0.2
$e^+e^- \to \ell^+\ell^-\nu\bar{\nu}(\gamma)$	1.80 ± 0.14
$e^+e^- \to e^+e^-\ell^+\ell^-$	1.2 ± 0.4
$e^+e^- \to \nu\bar{\nu}q\bar{q}$	0.71 ± 0.09
$e^+e^- \to \mu^+\mu^-(\gamma)$	0.37 ± 0.08
$e^+e^- \to \tau^+\tau^-(\gamma)$	0.17 ± 0.05
$e^+e^- \to \gamma\gamma(\gamma)$	$0.0 \ (< 0.05)$
Total physics background	4.6 ± 0.5
Cosmic background	2.6 ± 0.6
Beam related background	2.0 ± 1.4
Total background	9.2 ± 1.6

Table 2: Numbers of events expected from various background processes contributing to the single-photon event sample. The Standard Model background contributions are given by process. Also shown are the expected other backgrounds from cosmic rays and beam related sources. The errors shown are statistical.

Systematic	Relative Error(%)
Selection Efficiency	1.5
Occupancy probability	1.0
Early conversion	0.7
Tracking systematics	0.5
Event generator physics modelling	0.5
x_T scale and resolution	0.4
Integrated luminosity	0.2
Angular acceptance	0.2
MC statistics	0.2
Total	2.1

Table 3: Summary of the experimental systematic errors related to the efficiency and normalisation of the single photon cross-section measurement.

$\sqrt{s}$(GeV)	$\sigma_{\mathrm{meas}}^{\nu\bar{\nu}\gamma\gamma(\gamma)}$(pb)	$\sigma_{\mathrm{KORALZ}}^{\nu\bar{\nu}\gamma\gamma(\gamma)}$(pb)
130	1.49 ± 0.68	0.626 ± 0.010
136	1.23 ± 0.56	0.526 ± 0.008
161	0.16 ± 0.16	0.330 ± 0.018
172	0.32 ± 0.23	0.303 ± 0.017
183	0.27 ± 0.09	0.247 ± 0.002
189	0.20 ± 0.04	0.228 ± 0.002

Table 4: The measured cross-section for the process $e^+e^- \to \nu\bar{\nu}\gamma\gamma(\gamma)$, within the kinematic acceptance defined in section 3, for different centre-of-mass energies. For $\sqrt{s} = 130$ and 136 GeV the measurements are the weighted average of the results obtained from the 1997 data and the results obtained from the 1995 data. Results for $\sqrt{s} \leq 183$ GeV are taken from our previous publications [1, 2]. The final column shows the cross-section predictions from KORALZ. The quoted errors are statistical.

M_{X}	E_{min}	E_{max}	N_{obs}	N_{expected}	P_{fluct}	N^{95}	$\langle N^{95} \rangle$
100	25.1	97.6	390	449 ± 13	0.9921	23.4	52.6
110	30.5	97.7	371	428 ± 13	0.9917	22.9	51.0
120	36.3	97.9	358	407 ± 12	0.9832	24.1	49.5
130	42.6	98.1	342	386 ± 12	0.9768	24.4	48.0
140	49.3	98.4	320	364 ± 11	0.9812	23.0	46.4
150	56.5	98.7	293	340 ± 10	0.9899	20.6	44.6
160	64.0	99.3	258	303 ± 9	0.9915	19.0	41.7
170	71.6	100.1	152	182 ± 5	0.9844	15.4	31.5
180	78.8	101.9	15	15.3 ± 0.5	0.5615	9.3	10.0
185	81.4	104.0	7	6.2 ± 0.2	0.4213	7.6	7.1

Table 5: Results for $e^+e^- \to XY$, $X \to Y\gamma$, with $M_{\mathrm{Y}} \approx 0$. Shown are values for the mass M_{X}, the minimum and maximum energies (E_{min}, E_{max}) allowed by the kinematic consistency cuts, the number of observed events (N_{obs}), the number of events expected from $e^+e^- \to \nu\bar{\nu}\gamma(\gamma)$ (N_{expected}), the value of P_{fluct} as defined in Equation 4, the calculated 95% CL upper limit on the number of new-physics signal events (N^{95}), and the average value of N^{95} expected in the absence of signal ($\langle N^{95} \rangle$). Upper limits are calculated using the event-counting method. Masses and energies are in GeV.

δ	$\epsilon(\%)$	$\langle\sigma_{\mathrm{exp}}^{95}\rangle$ (fb)	σ^{95} (fb)	M_D lower limit (GeV)
2	76.5	241	309	1086
3	79.1	233	298	862
4	81.4	226	290	710
5	83.5	220	283	605
6	85.4	216	276	528
7	87.2	211	271	470

Table 6: Results for graviton-photon production in the context of extra dimensions. Shown are the number of extra dimensions δ, the efficiency ϵ, the average upper limit on the signal cross-section $\langle\sigma_{\mathrm{exp}}^{95}\rangle$ expected in the absence of signal, the measured 95% CL upper limit on signal cross-section σ^{95}, and the corresponding lower limit on the mass scale M_D. Efficiencies and cross-section limits are evaluated within the restricted kinematic acceptance described in Section 5.1.5.

M_{X}	$M_{\mathrm{Y}}=0$	$M_{\mathrm{Y}} = M_{\mathrm{X}}/2$	$M_{\mathrm{Y}} = M_{\mathrm{X}} - 10$	$M_{\mathrm{Y}} = M_{\mathrm{X}} - 5$	$M_{\mathrm{Y}} = M_{\mathrm{X}} - 2.5$
94	70.3 ± 1.2	70.7 ± 1.2	64.1 ± 1.3	38.9 ± 1.5	5.1 ± 0.7
90	69.4 ± 1.2	71.9 ± 1.2	60.4 ± 1.4	40.5 ± 1.5	4.6 ± 0.7
80	71.5 ± 1.2	69.3 ± 1.2	59.7 ± 1.4	39.5 ± 1.5	4.7 ± 0.7
70	71.0 ± 1.2	70.8 ± 1.2	60.4 ± 1.4	44.0 ± 1.5	4.4 ± 0.7
60	73.5 ± 1.1	71.1 ± 1.2	64.4 ± 1.3	42.5 ± 1.5	8.4 ± 0.9
50	69.8 ± 1.2	69.2 ± 1.2	65.1 ± 1.3	45.4 ± 1.5	10.0 ± 0.9

Table 7: Acoplanar-photons selection efficiencies (%) for the process $e^+e^- \to XX$, $X \to Y\gamma$ at $\sqrt{s} = 189$ GeV for various M_{X} and M_{Y} (in GeV), after application of kinematic-consistency cuts. These efficiency values are used to perform the efficiency parameterization across the $(M_{\mathrm{X}}, M_{\mathrm{Y}})$ plane. The errors shown are due to Monte Carlo statistics only. Efficiencies for the generated points at $M_{\mathrm{Y}} = 20$ and $M_{\mathrm{Y}} = M_{\mathrm{X}} - 15$ are not shown, but are similar to those for $M_{\mathrm{Y}} = 0$ and $M_{\mathrm{Y}} = M_{\mathrm{X}}/2$.

M_{X}	Selection efficiency	Selection efficiency with $M_{\mathrm{X}}^{\mathrm{max}} > M_{\mathrm{X}} - 5$ GeV	N_{data}	$N_{\nu\bar{\nu}\gamma\gamma(\gamma)}$
94	72.2 ± 1.2	70.4 ± 1.2	3	1.34 ± 0.07
90	71.3 ± 1.2	67.5 ± 1.3	5	2.40 ± 0.09
80	72.3 ± 1.2	68.7 ± 1.4	7	4.81 ± 0.13
70	71.4 ± 1.2	69.2 ± 1.2	9	7.22 ± 0.15
60	74.0 ± 1.1	71.1 ± 1.2	11	10.05 ± 0.18
50	70.2 ± 1.2	67.7 ± 1.3	14	13.67 ± 0.20

Table 8: Acoplanar-photons event selection efficiencies (%), as a function of mass, for the process $e^+e^- \to XX$, $X \to Y\gamma$, for $M_{\mathrm{Y}} \approx 0$ at $\sqrt{s} = 189$ GeV. The first column shows the efficiency of the selection described in section 3.2. The second column shows the efficiency (%) after the additional cut on $M_{\mathrm{X}}^{\mathrm{max}}$. The third column shows the number of selected events consistent with the mass value M_{X}. The last column shows the expected number of events from the process $e^+e^- \to \nu\bar{\nu}\gamma\gamma(\gamma)$ (KORALZ). The errors shown due to from Monte Carlo statistics only.

$\log_{10}(\tau_X)$	Selection efficiency with $M_X^{\max} > M_X - 5$ GeV			
	M_X=50 GeV	M_X=75 GeV	M_X=90 GeV	M_X=94 GeV
-15	65.2 ± 1.7	68.2 ± 1.6	71.1 ± 1.5	72.1 ± 1.5
-10	63.3 ± 1.8	67.8 ± 1.6	72.2 ± 1.5	71.4 ± 1.5
-9	59.9 ± 1.8	71.7 ± 1.6	71.3 ± 1.6	72.1 ± 1.6
-8.3	25.8 ± 1.7	43.5 ± 4.0	49.7 ± 4.8	51.4 ± 5.6
-8	13.9 ± 1.5	25.8 ± 3.0	33.0 ± 3.8	37.8 ± 3.7
-7.3	2.5 ± 1.1	2.7 ± 1.0	5.6 ± 1.1	10.7 ± 2.4
-7	0.8 ± 1.0	1.0 ± 0.9	2.2 ± 1.0	5.1 ± 1.2
N_{data}	14	7	5	3
$N_{\nu\bar{\nu}\gamma\gamma(\gamma)}$	13.67 ± 0.20	5.88 ± 0.14	2.40 ± 0.09	1.34 ± 0.07

Table 9: Acoplanar-photons event selection efficiencies (%), as a function of mass M_X, and lifetime τ_X for the process $e^+e^- \to XX$, $X \to Y\gamma$, for $M_Y \approx 0$ at $\sqrt{s} = 189$ GeV. The uncertainties in the selection efficiencies include the contributions due to the limited Monte Carlo signal sample size, the variation of the timing cuts, and the parameterisation of the fit efficiencies. Also included are the number of events found in the data and the number expected from the $e^+e^- \to \nu\bar{\nu}\gamma\gamma(\gamma)$ background that are consistent with the kinematic consistency cut for the M_X mass values considered.
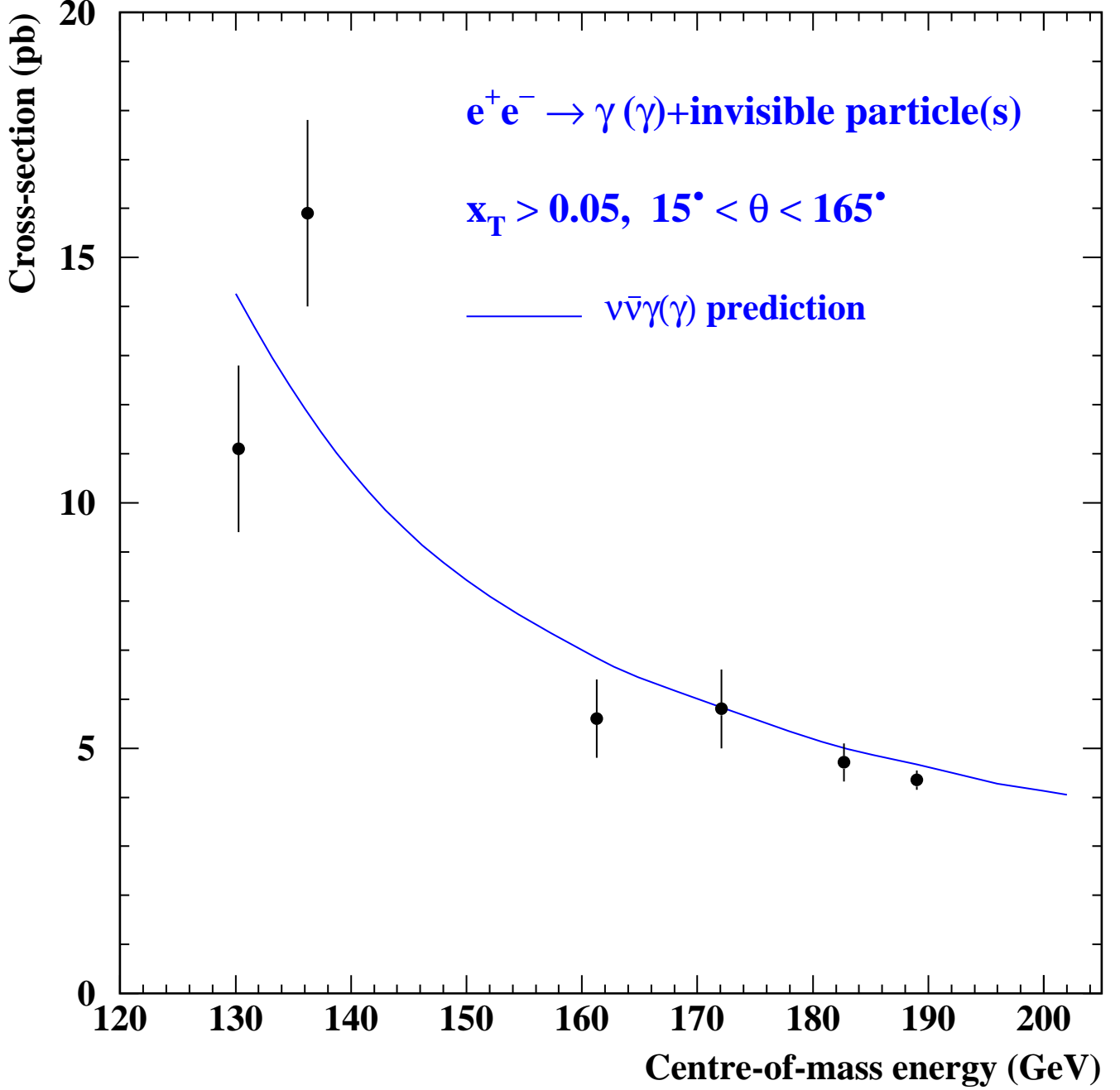
Figure 1: The measured value of $\sigma(e^+e^- \to \gamma(\gamma) + \text{invisible particle(s)})$, within the kinematic acceptance of the single-photon selection, as a function of $\sqrt{s}$. The data points with error bars are OPAL measurements at $\sqrt{s} = 130, 136, 161, 172, 183$ and 189 GeV. The curve is the prediction for the Standard Model process $e^+e^- \to \nu\bar{\nu}\gamma(\gamma)$ from the KORALZ generator.

OPAL
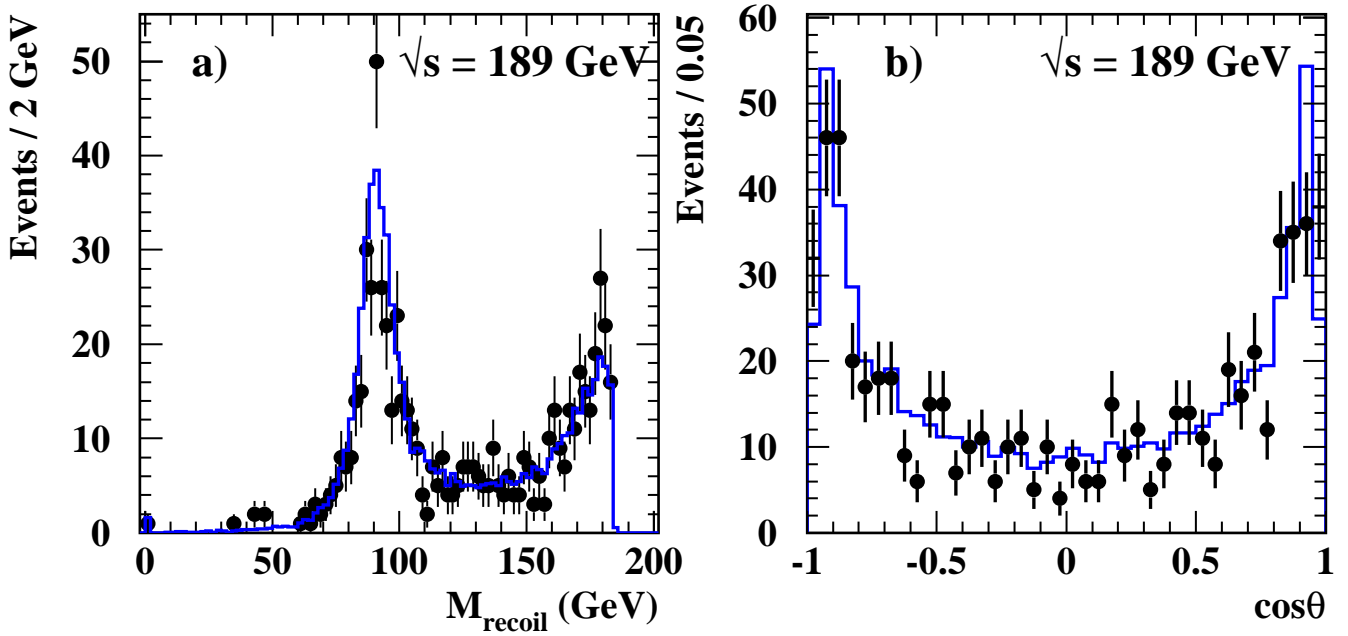
Figure 2: a) The recoil mass distribution for events passing the single-photon selection for the $\sqrt{s} = 189$ GeV data sample. b) The $\cos\theta$ distribution for the most energetic photon in the single-photon selection at $\sqrt{s} = 189$ GeV. In both plots, the points with error bars are the data and the histogram is the expectation from the KORALZ $e^+e^- \to \nu\overline{\nu}\gamma(\gamma)$ Monte Carlo normalized to the integrated luminosity of the data.

OPAL
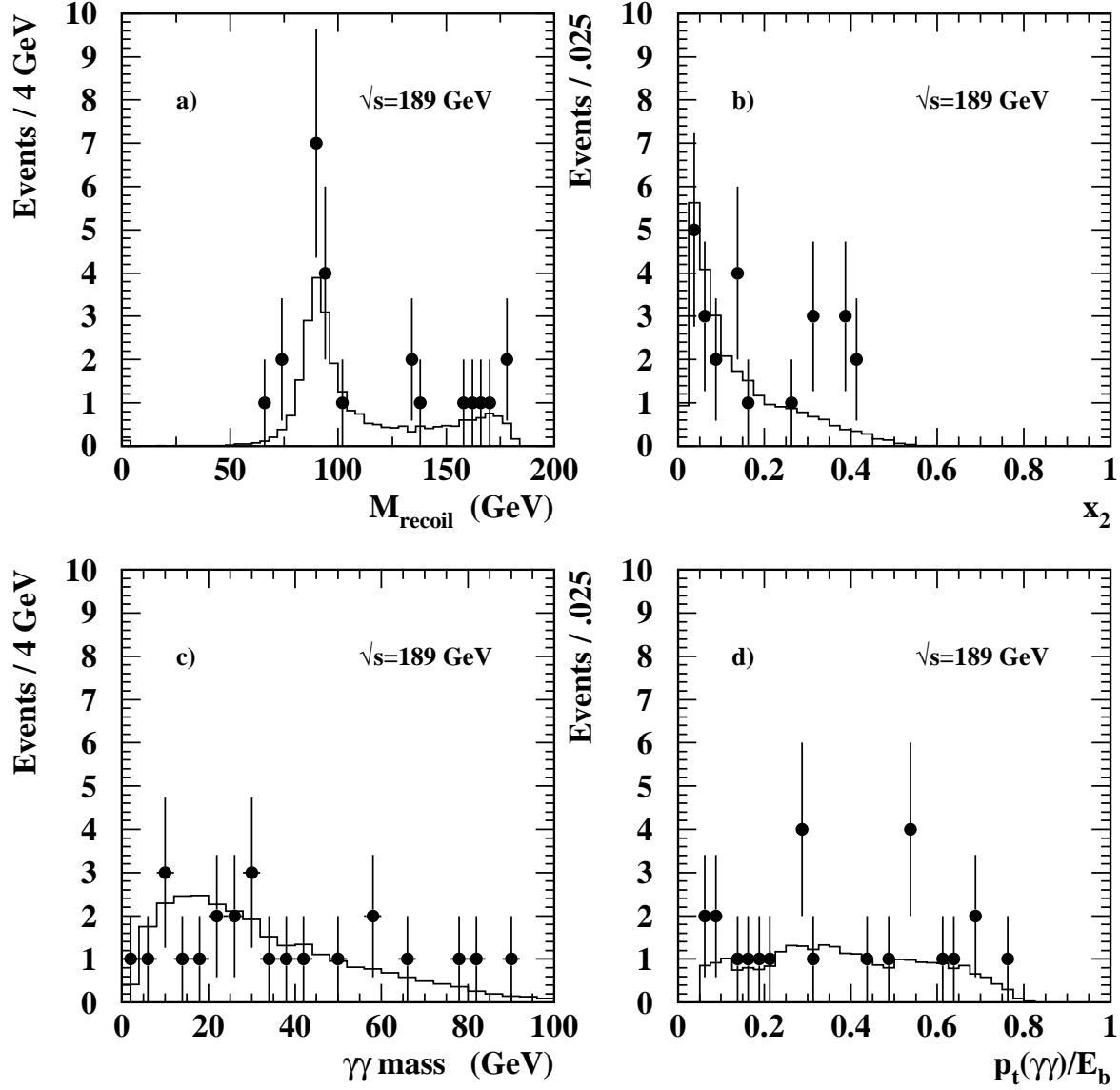
Figure 3: Plots of kinematic quantities for the selected acoplanar-photons events for $\sqrt{s} = 189$ GeV. a) Recoil-mass distribution. b) Distribution of the scaled energy of the second photon (x_2). c) Distribution of the invariant mass of the $\gamma\gamma$ system. d) Scaled transverse momentum distribution for the $\gamma\gamma$ system. The data points with error bars represent the selected OPAL data events. In each case the histogram shows the expected contribution from $e^+e^- \rightarrow \nu\bar{\nu}\gamma\gamma(\gamma)$ events, from KORALZ, normalized to the integrated luminosity of the data.
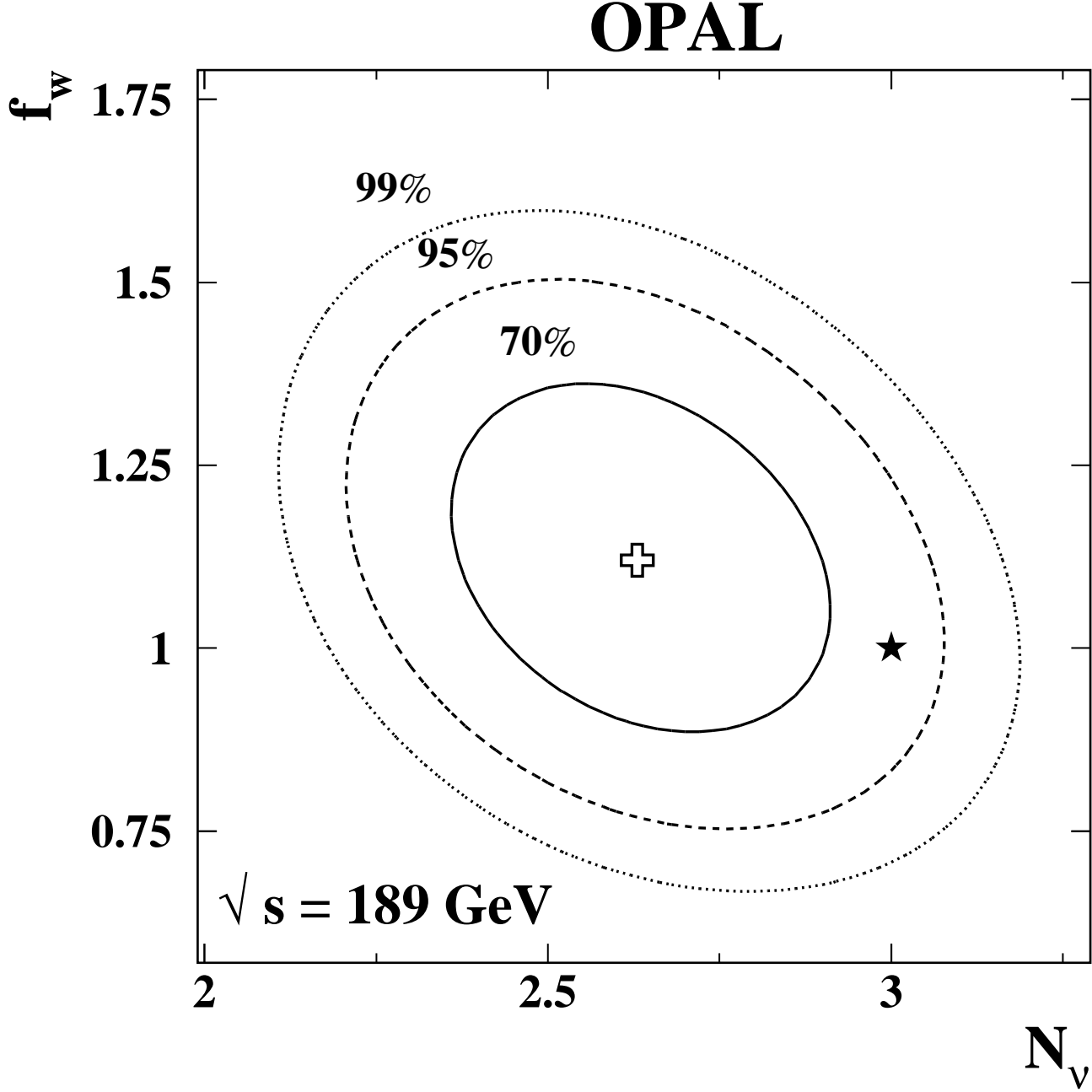
Figure 4: The 70%, 95% and 99% confidence level contours in the f_W, N_ν plane resulting from the likelihood fit to the overall rate and the photon energy spectrum measured in the single-photon selection. The cross indicates the central values of the fit results, while the Standard Model expectation (N_ν=3, f_W=1) is shown by the star.
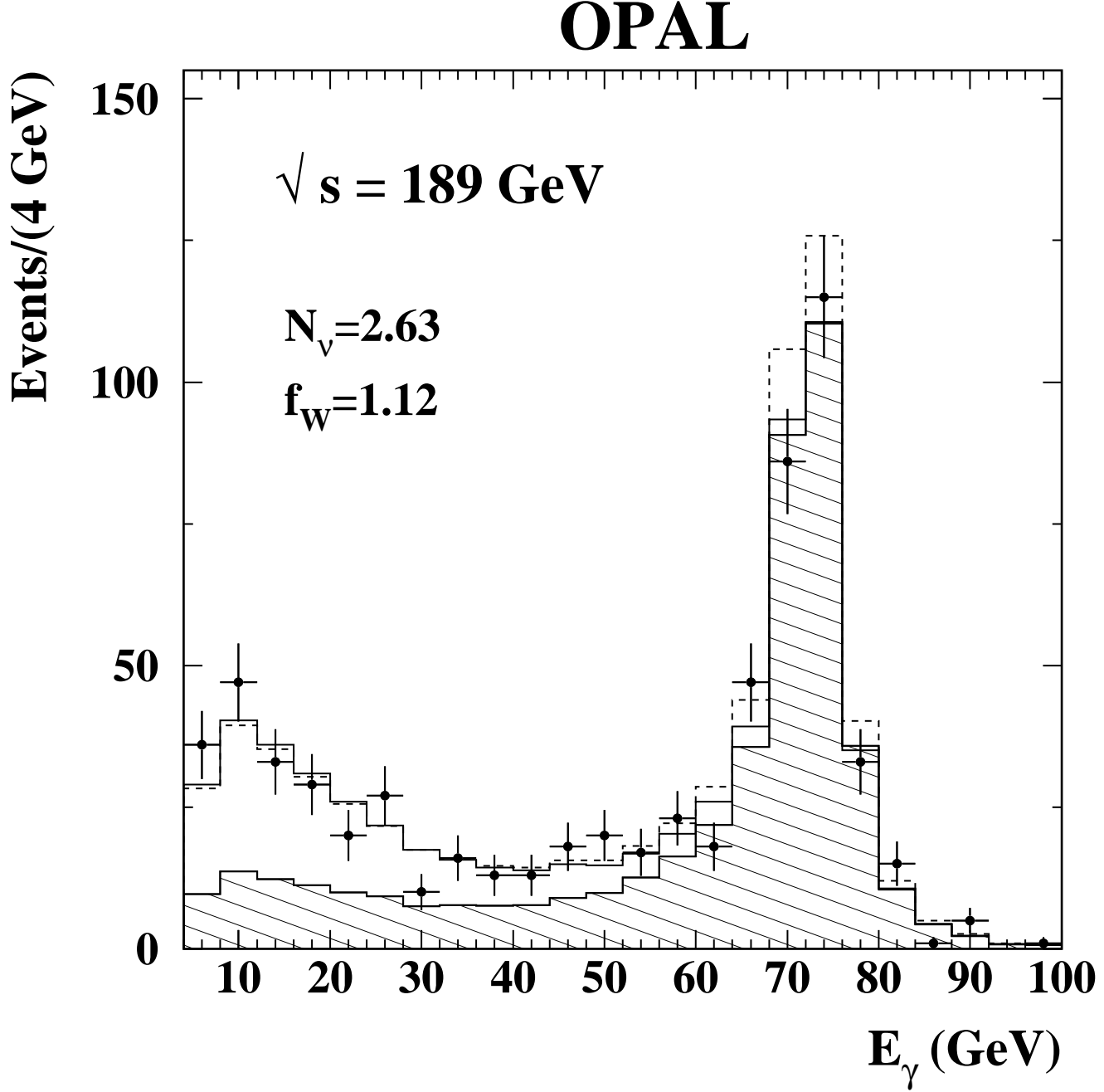
Figure 5: Photon energy distributions for single-photon events. The points with error bars are the data. The solid histogram is the prediction for the values $f_W = 1.12$, $N_\nu = 2.63$ most consistent with the data. The dashed histogram is the expectation for the Standard Model values $f_W = 1$, $N_\nu = 3$. The hatched region indicates the pure s-channel Z^0 contribution for $N_\nu = 2.63$. All predicted distributions were calculated using the NUNUGPV98 generator.
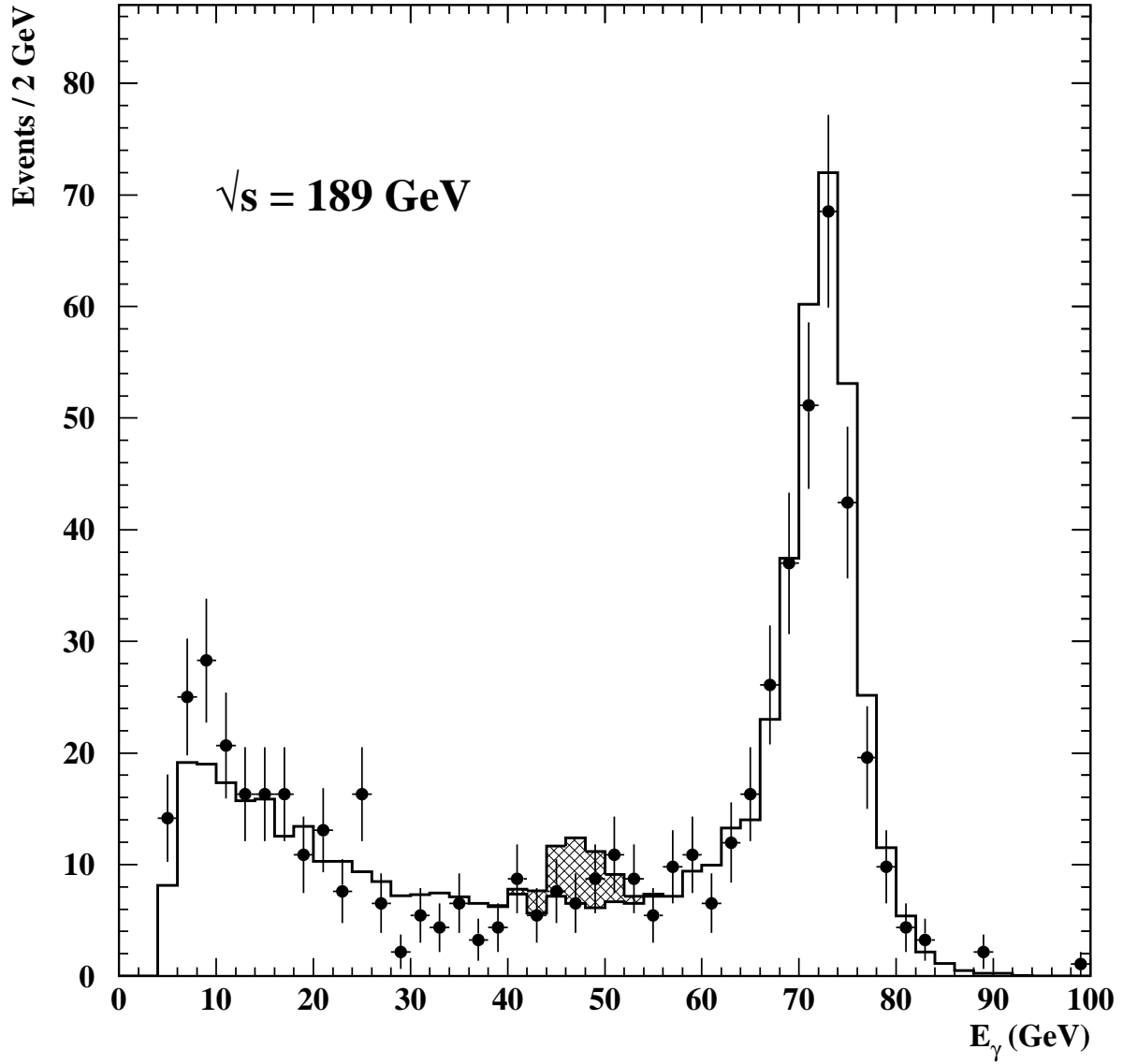
Figure 6: The observed single-photon energy distribution after application of the degraded-resolution cuts. The data are shown as the points with error bars and are compared with the expectation from the Standard Model process $e^+e^- \rightarrow \nu\overline{\nu}\gamma(\gamma)$, evaluated with KORALZ. The extra hatched contribution around 45 GeV illustrates the expected additional contribution from XY production which is excluded at 95% CL using the event-counting method for particular X and Y masses. The hatched contribution corresponds to M_X=125 GeV and M_Y=63 GeV with a cross-section times branching ratio of 142 fb.

OPAL
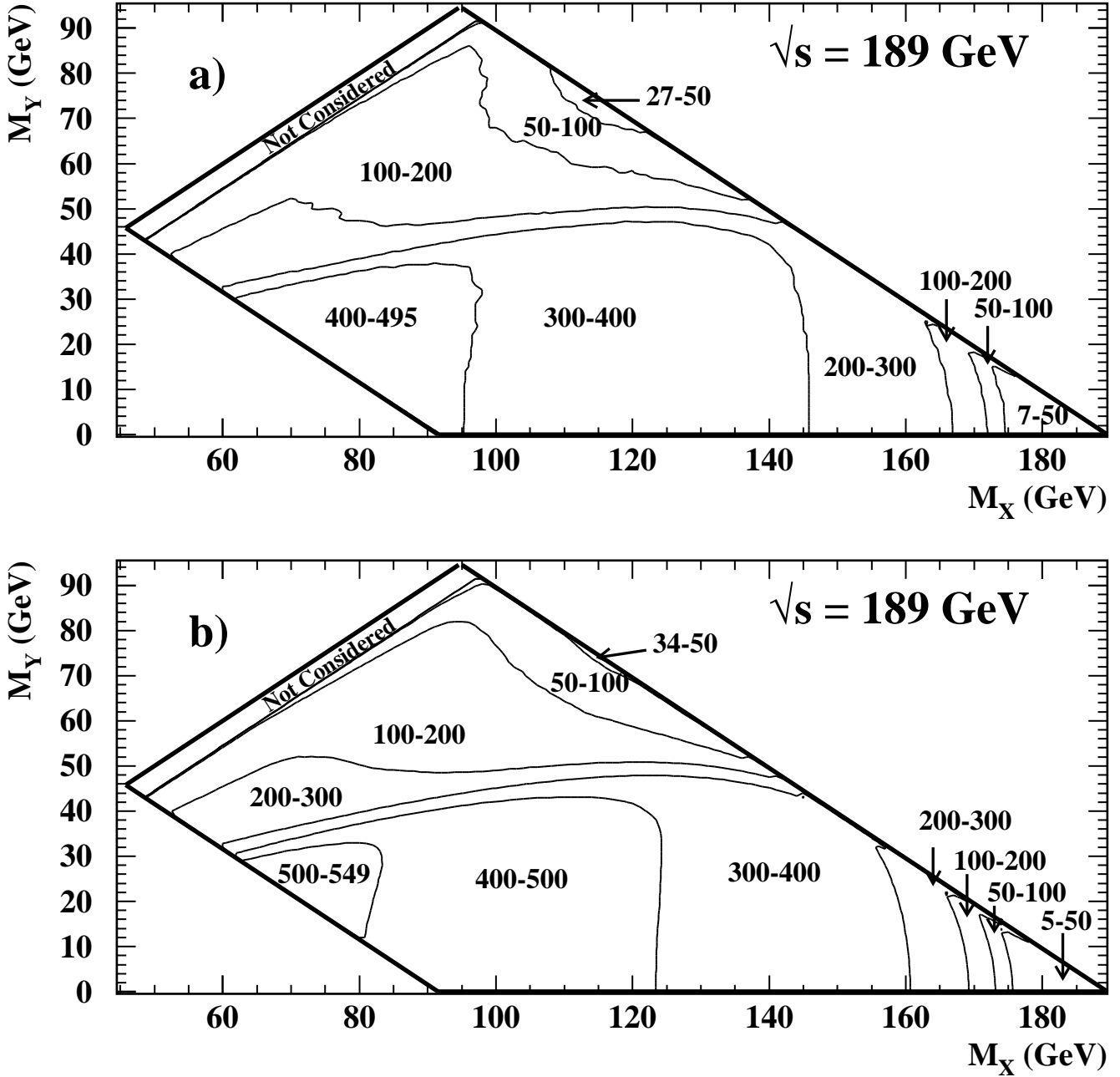
Figure 7: Contour plots for the $\sqrt{s} = 189$ GeV data sample search for $e^+e^- \to XY$, $X \to Y\gamma$, after application of both degraded-resolution and kinematic-consistency cuts. For each set of mass values (M_X, M_Y), a) shows the range of numbers of observed single-photon candidate events between each contour and b) shows the range of numbers of expected events from $e^+e^- \to \nu\bar{\nu}\gamma(\gamma)$ between each contour. The $\nu\bar{\nu}\gamma(\gamma)$ expectation was derived using KORALZ. Lines are drawn around the boundaries defined by $M_X + M_Y = 189$ GeV, $M_X = M_Y$, and $M_X + M_Y = M_Z$. The region in which $M_X - M_Y < 5$ GeV is not considered.
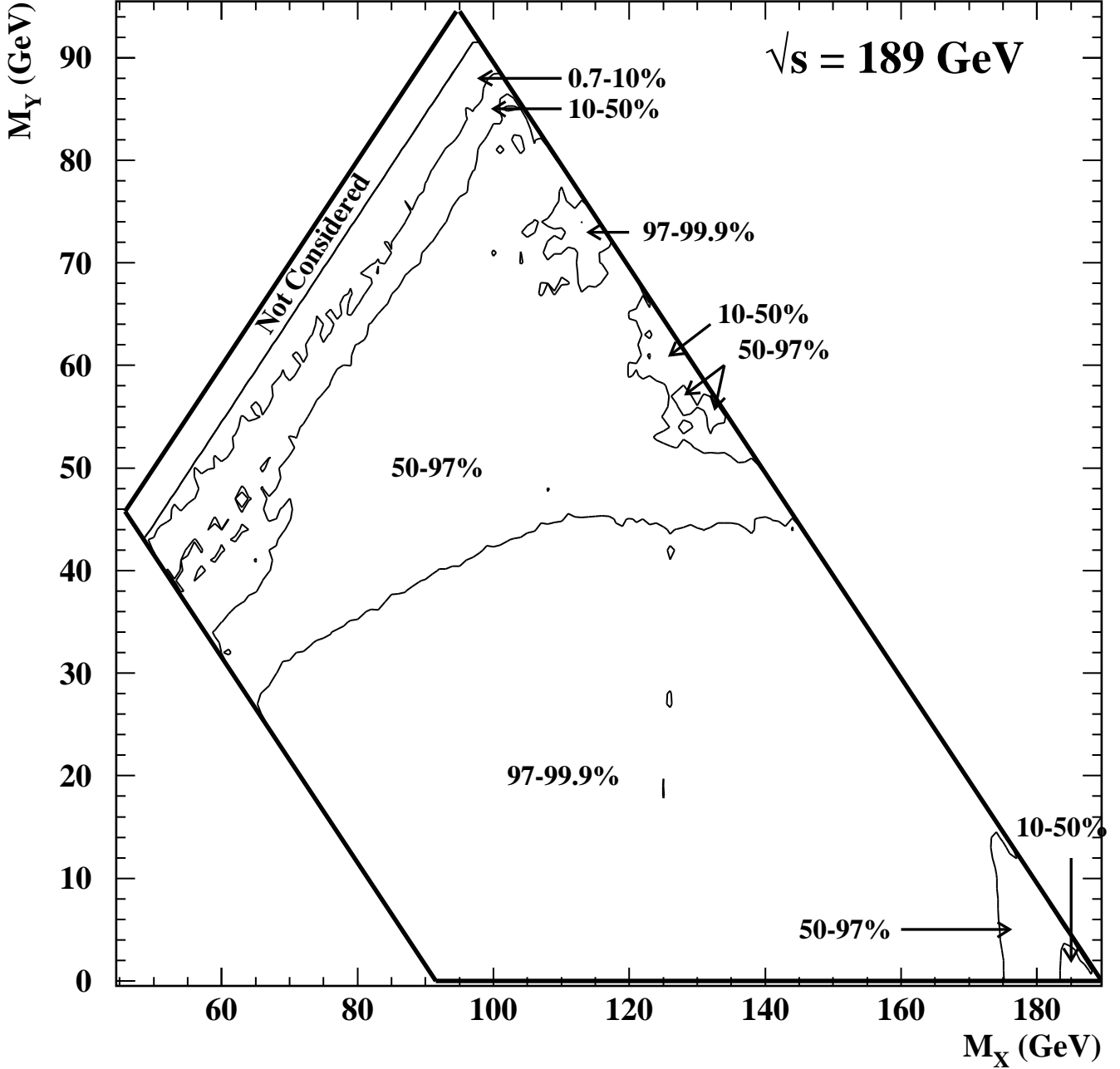
Figure 8: Consistency between the number of observed events and the number of events expected from $e^+e^- \rightarrow \nu\bar{\nu}\gamma(\gamma)$ as estimated by KORALZ. Plotted is the probability for the number of expected events to fluctuate to the number of observed events or more, as described in the text. Values greater than 50% indicate a downward fluctuation where the number of observed events is fewer than expected. The boundaries and delineated regions are as defined for Figure 7.
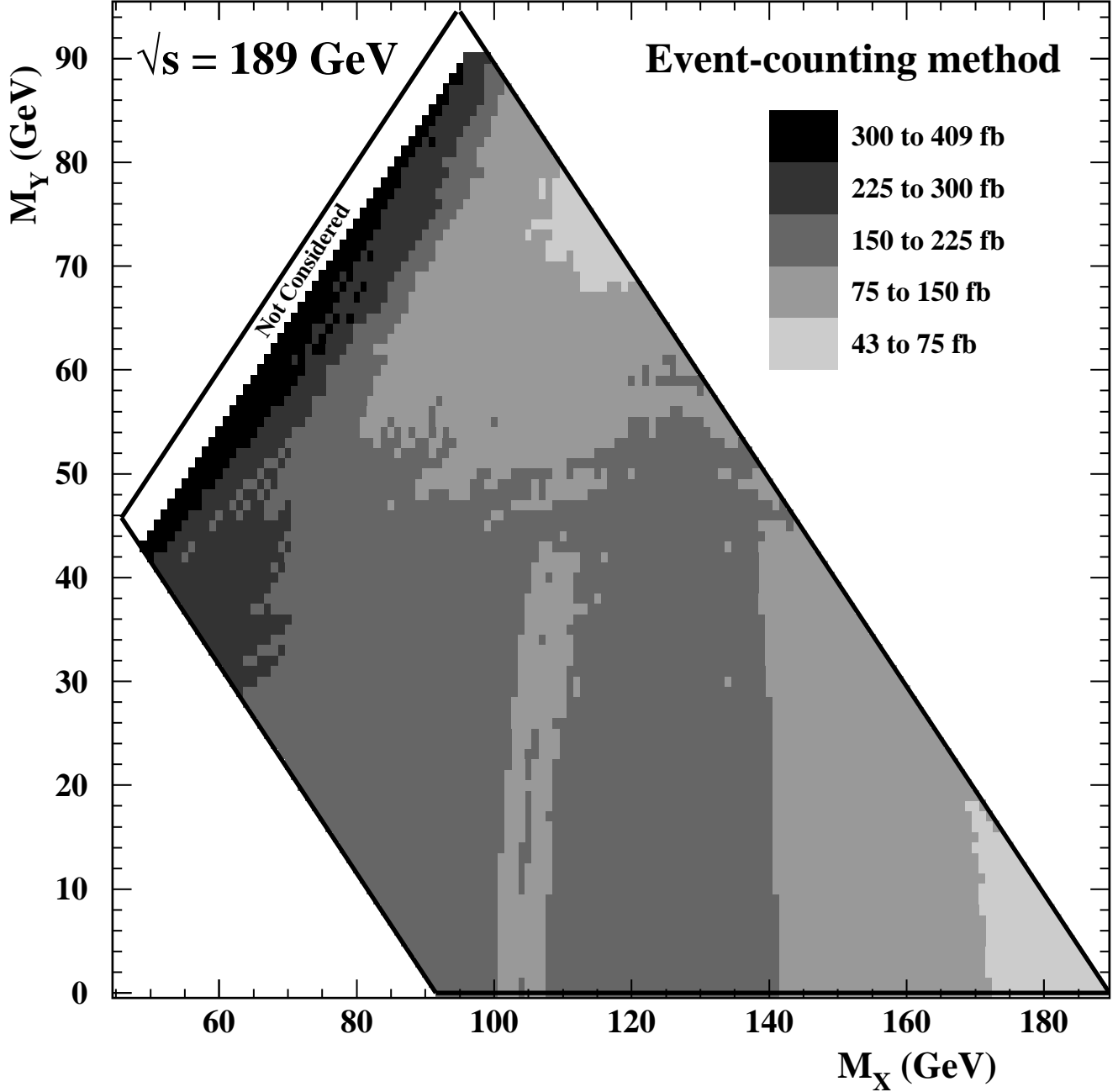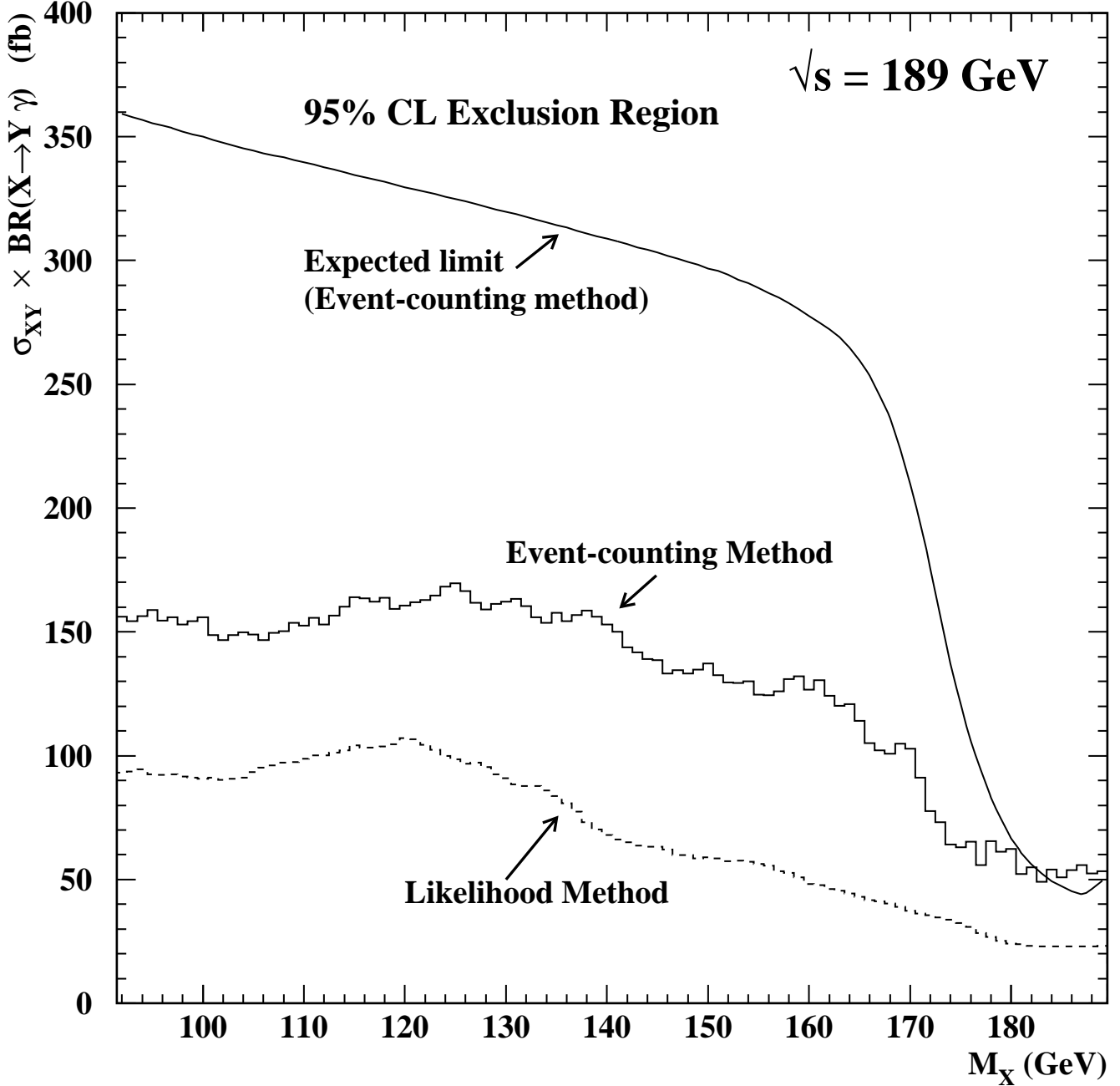
Figure 9: The 95% CL upper limit on $\sigma(e^+e^- \to XY) \cdot BR(X \to Y\gamma)$ at $\sqrt{s} = 189$ GeV as a function of M_X and M_Y, using the event-counting method described in the text. The boundaries and delineated regions are as defined for Figure 7.
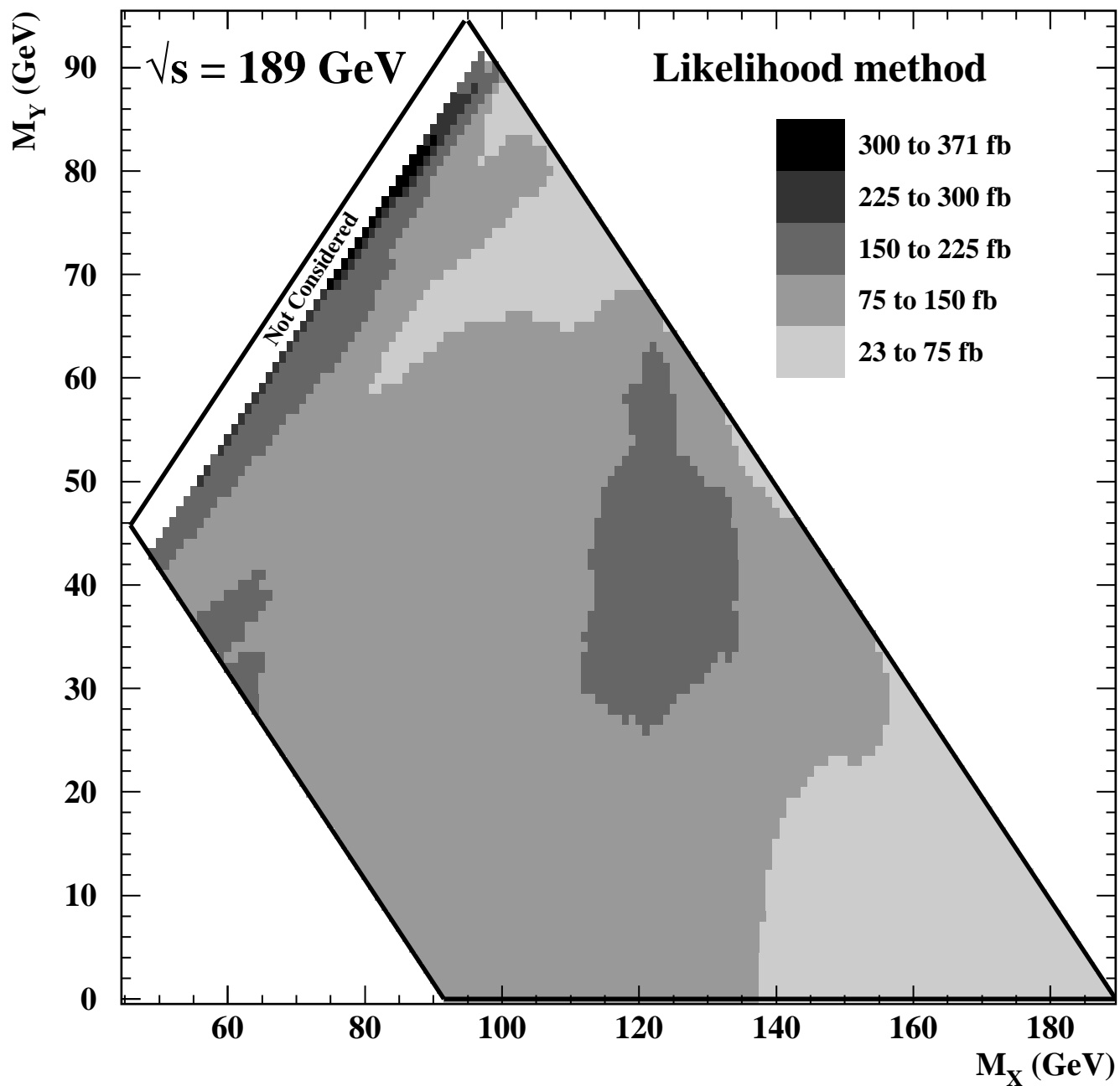
OPAL

Figure 10: The 95% CL upper limit on $\sigma(e^+e^- \to XY) \cdot BR(X \to Y\gamma)$ at $\sqrt{s} = 189$ GeV as a function of M_X and M_Y, using the likelihood-based method described in the text. The boundaries and delineated regions are as defined for Figure 7.

OPAL

Figure 11: The 95% CL upper limits on $\sigma(e^+e^- \to XY) \cdot BR(X \to Y\gamma)$ at $\sqrt{s} = 189$ GeV as a function of M_X, assuming $M_Y \approx 0$, calculated using the likelihood-based method and the event-counting method as described in the text. Also shown is the average limit expected in the absence of signal, calculated using the event-counting method.
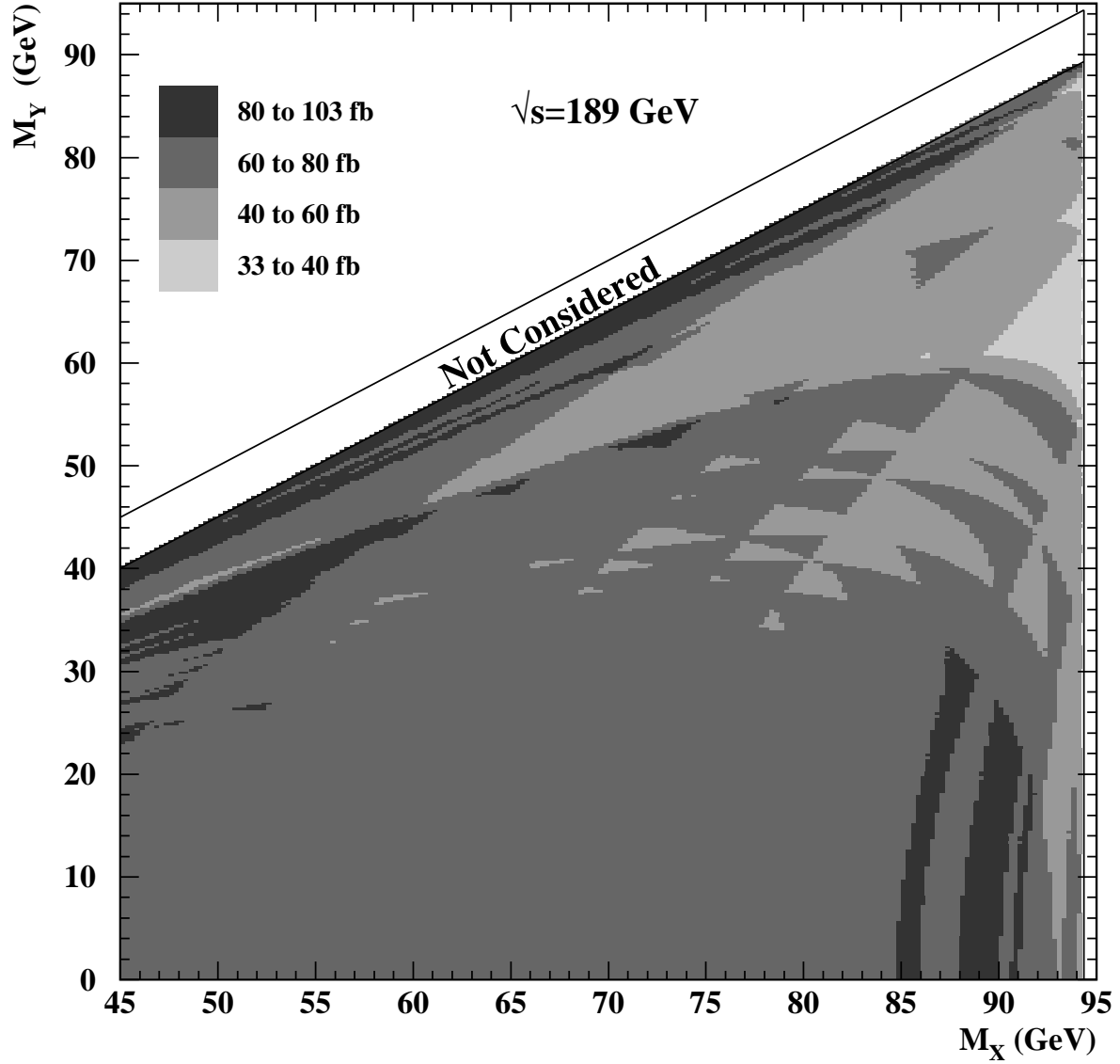
Figure 12: The shaded areas show 95% CL exclusion regions for $\sigma(\mathrm{e^+e^-} \to \mathrm{XX}) \cdot \mathrm{BR}^2(\mathrm{X} \to \mathrm{Y}\gamma)$ at $\sqrt{s} = 189$ GeV. No limit is set for mass-difference values $M_\mathrm{X} - M_\mathrm{Y} < 5$ GeV, defined by the lower line above the shaded regions. The upper line is for $M_\mathrm{X} = M_\mathrm{Y}$.
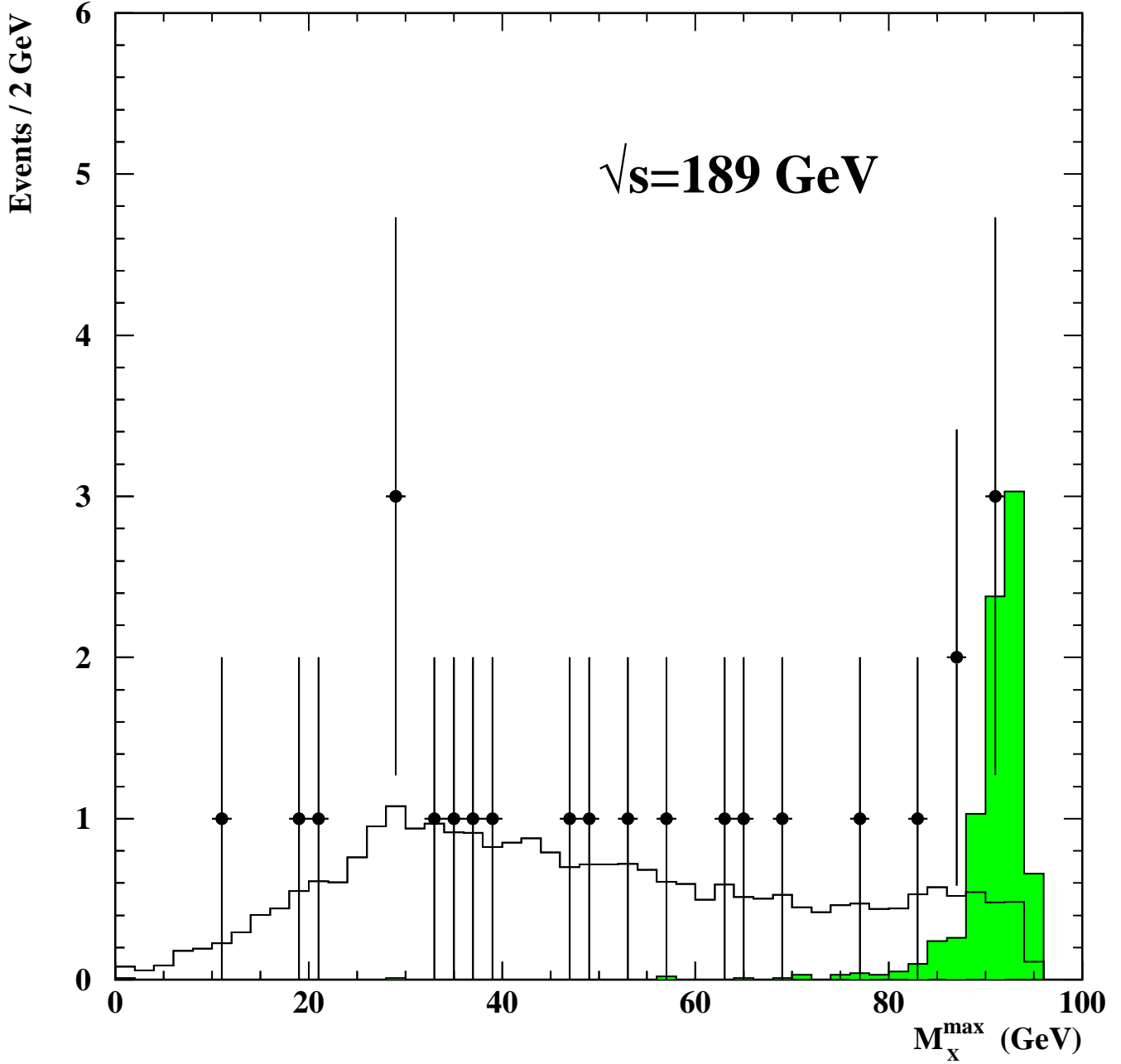
Figure 13: M_X^{max} distribution of the selected acoplanar-photons events (points with error bars). Shown as an unshaded histogram is the expected distribution from the Standard Model process $e^+e^- \to \nu\bar{\nu}\gamma\gamma(\gamma)$, evaluated using KORALZ and normalized to the integrated luminosity of the data. The shaded histogram shows the expected distribution for the signal process $e^+e^- \to XX$, $X \to Y\gamma$ for $M_X = 90$ GeV with arbitrary production cross-section.
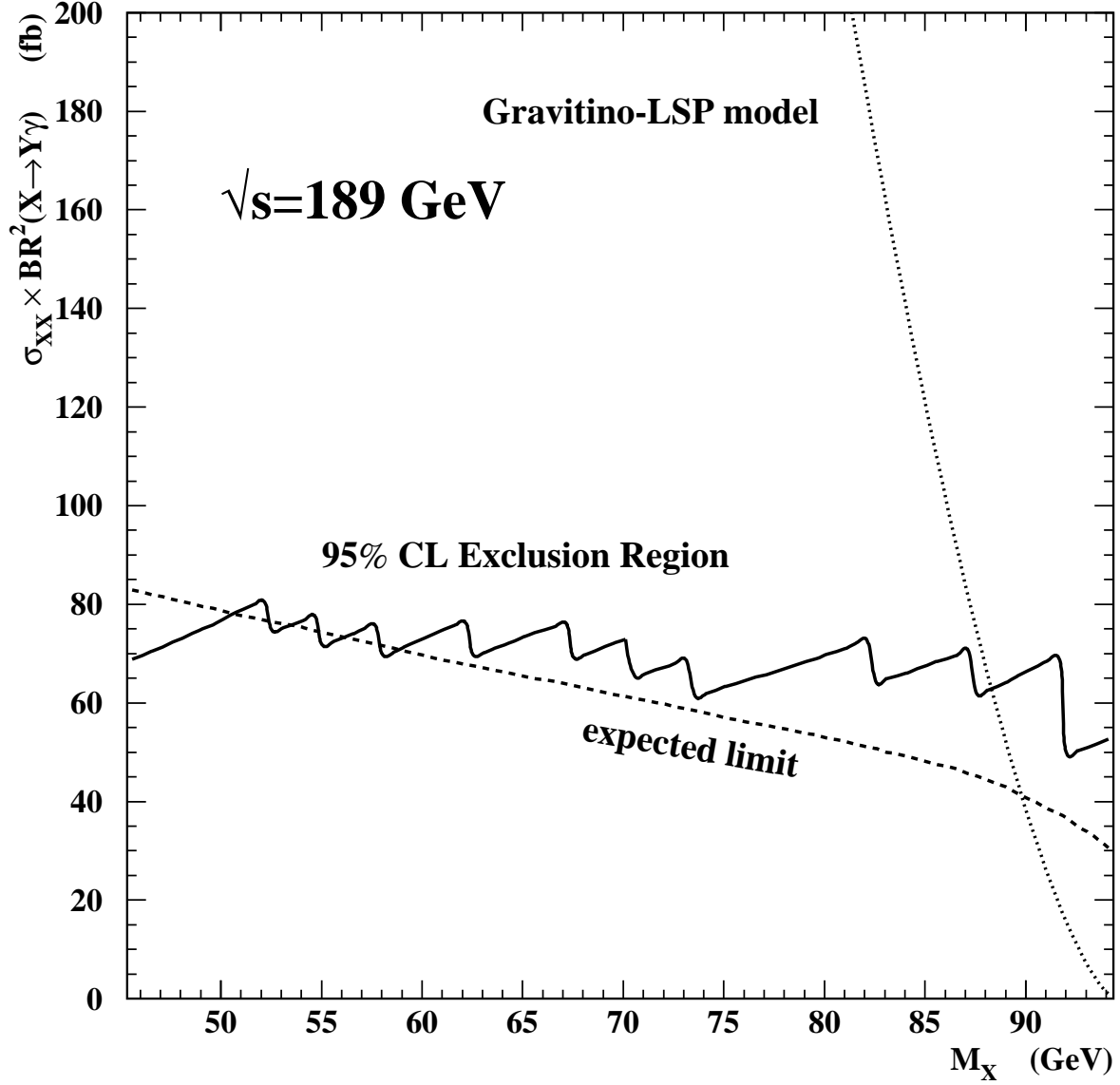
Figure 14: 95% CL upper limit on $\sigma(e^+e^- \to XX) \cdot BR^2(X \to Y\gamma)$ for $M_Y \approx 0$ (solid line). Also shown is the expected limit (dashed line). The dotted line shows the cross-section prediction of a specific light gravitino LSP model [30]. Within that model, $\tilde{\chi}_1^0$ masses between 45 and 88.3 GeV are excluded at the 95% CL. These limits assume that particle X decays promptly.
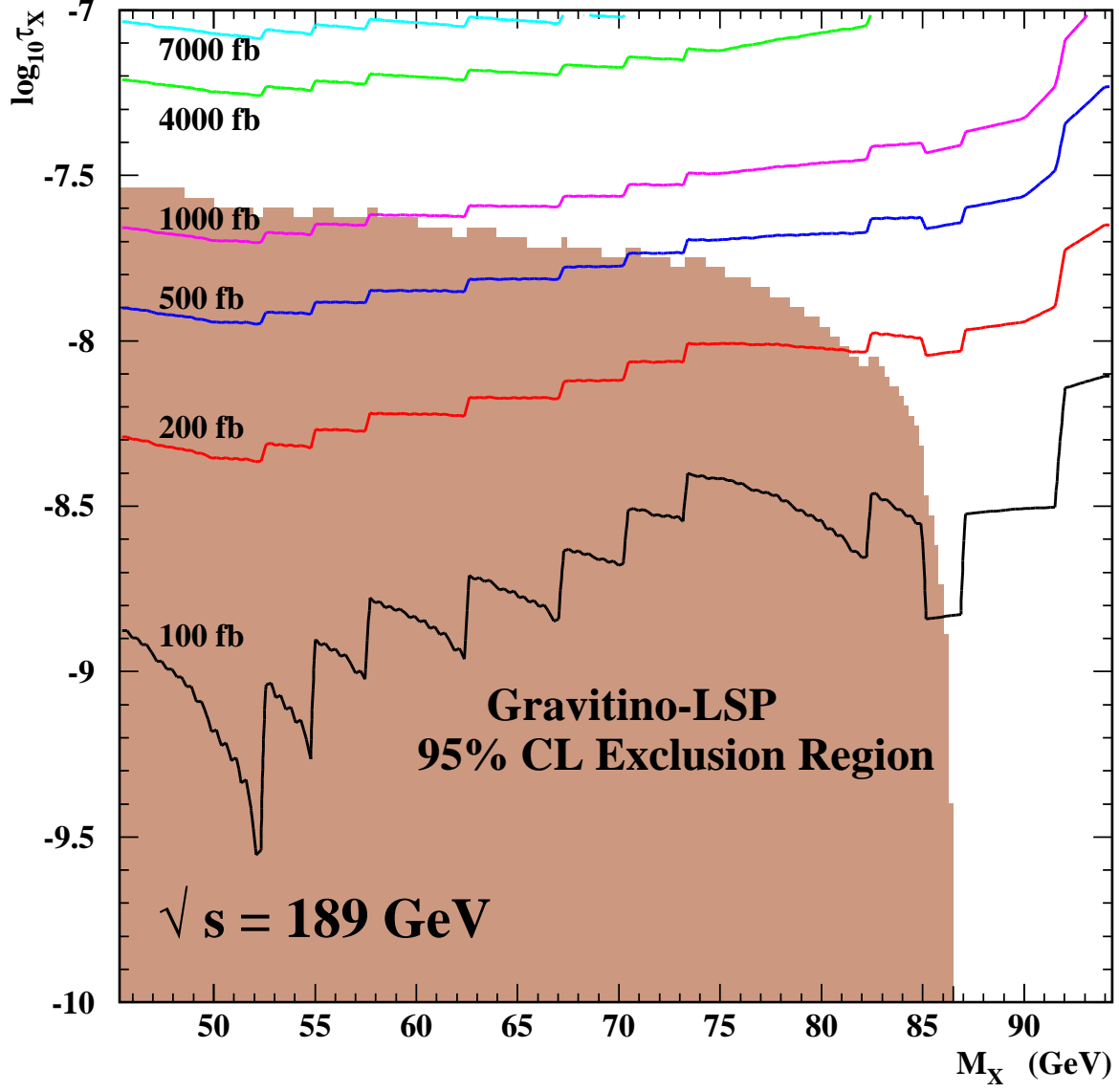
Figure 15: The 95% CL upper limit on $\sigma(e^+e^- \to XX) \cdot BR^2(X \to Y\gamma)$ for $M_Y \approx 0$ as a function of M_X and $\log_{10}(\tau_X)$ (with τ_X in seconds), calculated using the efficiencies of Table 9 to extend the predictions of Figure 14 to the case of X with a non-negligible decay length. Superimposed is the domain defined by the 95% CL exclusion limit (shaded region) under the assumption of a light gravitino LSP model [30].